Effects of filler size on the curing mechanism of allyl-functionalized preceramic polymer

Latheef MA, Porobic Katnic S, LePage W, Keller MW, Ramsurn H

PUBLISHED AS

Latheef MA, Porobic Katnic S, LePage W, Keller MW, Ramsurn H. “Effects of filler size on the curing mechanism of allyl-functionalized preceramic polymer.” Journal of Thermal Analysis and Calorimetry (2026).

https://doi.org/10.1007/s10973-026-16041-x

Effects of Filler Size on the Curing Mechanism of Allyl-Functionalized Preceramic Polymer

Mohammed Ammar Abdul Latheef[1], Slavica Porobic Katnic[2,3], William LePage[2], Michael W. Keller[2], and Hema Ramsurn[1†]

[1]The Russell School of Chemical Engineering, University of Tulsa, Tulsa, OK, 74104, USA
[2]Department of Mechanical Engineering, University of Tulsa, Tulsa, OK, 74104, USA
[3]University of Belgrade, Vinča Institute of Nuclear Sciences, National Institute of the Republic of Serbia, Belgrade, 11000, Serbia
[†]Correspondence: hema-ramsurn@utulsa.edu

Abstract

Silicon carbide (SiC) particle incorporation is widely employed in polymer infiltration and pyrolysis processing to enhance densification and reduce shrinkage of preceramic polymer matrices. However, its influence on curing kinetics remains insufficiently understood. This study investigates how SiC filler size and loading affect the non-isothermal curing behavior of SMP-10, an allylhydridopolycarbosilane and a common precursor for SiC-based ceramic matrix composites. SMP-10 formulations containing micro- and nano-sized SiC particles at particle-to-polymer mass ratios of 0.1–0.3 were analyzed using differential scanning calorimetry at heating rates of 0.5–10 °C min^{-1}. Activation energies were determined using Kissinger and Ozawa peak-based methods together with model-free isoconversional methods (Kissinger–Akahira–Sunose (KAS), Flynn–Wall–Ozawa (FWO), and Starink). Master plot analysis was subsequently applied to identify dominant reaction mechanisms. Micro-SiC addition decreased the apparent activation energy compared with pure SMP-10. The average activation energy obtained from the KAS method decreased from ~ 116 kJ mol^{-1} for pure SMP-10 to 92.5, 88.5, and 85.8 kJ mol^{-1} at micro-SiC loadings of 0.1, 0.2, and 0.3. In contrast, nano-SiC increased the apparent activation energy and introduced stronger conversion dependence, accompanied by systematic shifts of the curing exotherms toward higher temperatures. Master plot analysis indicated Avrami–Erofeev nucleation and growth kinetics for micro-filled systems, whereas nano-filled formulations exhibited reaction-order behavior at higher loadings. Despite these kinetic differences, the Gibbs free energies of activation remained within a relatively narrow range across all formulations. From a processing perspective, these findings provide guidance for selecting filler size and loading to tailor curing schedules in particle-modified SMP-10 systems used in PIP-derived SiC matrix composites.

Keywords: Polymer-derived ceramics, SMP-10, Silicon carbide fillers, Curing kinetics, Isoconversional analysis, Polymer infiltration and pyrolysis

1 Introduction

Ceramic matrix composites (CMCs) have attracted significant attention as structural materials and protective coatings for extreme environments due to their ability to combine the intrinsic advantages of ceramics with enhanced damage tolerance provided by fiber reinforcement[1,2]. In these systems, ceramic or carbon fibers reinforce a ceramic matrix and reduce the brittle fracture typical of monolithic ceramics such as alumina, silicon carbide, and zirconia, where failure often originates from surface flaws and microcrack formation under severe thermal gradients and mechanical loading[3–5]. The resulting composites have improved fracture toughness and reliability while retaining key properties including high stiffness, thermal stability, low thermal expansion, moisture resistance, and chemical durability[6]. The relevance of CMCs is particularly evident in applications where conventional materials fail to meet performance requirements. Components operating in aero-engine hot sections[7], rocket propulsion systems[6], and hypersonic flight structures are routinely exposed to extreme temperatures and aggressive environments, making CMCs suitable for

thermal components, nozzles, and aerodynamic shells[2,8]. Consequently, considerable research has focused on scalable and reliable processing routes for SiC-based CMCs. Among these approaches, the Polymer Infiltration and Pyrolysis (PIP) method remains one of the most versatile fabrication strategies[9]. PIP enables infiltration of complex fiber preforms with liquid preceramic polymers and is compatible with particulate additions and complementary densification methods[10]. During processing, a porous fiber preform is impregnated with a liquid preceramic polymer that is subsequently crosslinked through curing and converted into a ceramic phase during pyrolysis in an inert atmosphere[11]. Despite these advantages, polymer-to-ceramic conversion is accompanied by significant mass loss and volumetric shrinkage[12], resulting in residual porosity and necessitating multiple infiltration–pyrolysis cycles to achieve adequate densification[13–15].

Polycarbosilanes (PCS) are widely used preceramic polymers for SiC matrix formation and are typically derived from polydimethylsilane-based precursors[16,17]. PCS pyrolysis yields silicon carbide at elevated temperatures, but residual free carbon and oxygen may remain and affect crystallinity, mechanical performance, and oxidation resistance[18,19]. Partially allyl-substituted hydridopolycarbosilane (AHPCS) has therefore been developed as an alternative precursor offering improved compositional control and favorable processing characteristics for carbon fiber–reinforced SiC composites[12,20]. The present study focuses on SMP-10, a commercially available AHPCS precursor widely employed in C_f/SiC composite fabrication. Despite its processing advantages, SMP-10 exhibits a relatively high thermal curing temperature of approximately 250 °C in the absence of catalysts or initiators[15]. Such elevated curing temperatures increase energy consumption and may introduce thermal stresses during processing, potentially leading to microcracking or delamination[7]. Therefore, improved control over SMP-10 curing behavior is necessary to improving composite processing reliability[21]. For AHPCS systems, curing involves concurrent hydrosilylation, dehydrocoupling, and possible radical-mediated reactions, typically occurring between 140 and 250 °C[5,19,22]. The sensitivity of these reactions to processing conditions highlights the importance of understanding factors that influence curing kinetics.

Low-temperature curing using radical initiators has been reported previously[23] , whereas alternative non-chemical approaches have received less attention. The incorporation of inert ceramic fillers into preceramic polymers provides a route to reduce shrinkage and porosity during polymer-to-ceramic conversion[24,25] . In particular, silicon carbide particles reduce the fraction of shrinkage-prone polymer, improve packing efficiency, and promote earlier pore closure during pyrolysis, which improves densification efficiency[26,27]. The addition of filler particles is strongly influenced by particle size and associated densification mechanisms. Nanoscale SiC powders are frequently used in nano-infiltration and transient eutectoid (NITE) processing, where they contribute directly to matrix formation through sintering-assisted mechanisms[28]. In contrast, particle-enhanced PIP approaches typically employ fine or submicron SiC particles as inert fillers that primarily influence packing behavior and shrinkage evolution. These distinctions suggest that micro- and nanoscale particles may affect polymer curing through different physical mechanisms, including interfacial interactions and transport processes[25,29]. Beyond chemical modification strategies, particulate incorporation may influence curing through physical effects such as altered heat transfer, restricted chain mobility, and polymer–particle interfacial interactions[30,31]. Studies in thermoset systems have demonstrated that filler size and loading can affect apparent activation energies and transitions between chemically and diffusion-controlled regimes under non-isothermal conditions[32]. Despite the widespread use of SiC fillers in polymer-derived ceramic systems, the influence of filler particle size on the curing kinetics and thermodynamic parameters of SMP-10 has not been systematically investigated.

Previous studies have investigated the curing behavior of polysilazanes and siloxane-based preceramic polymers, typically focusing on overall activation energies or qualitative shifts in curing temperature. In particular, it remains unclear whether the presence of SiC fillers alters the intrinsic curing chemistry of SMP-10 or whether the observed changes arise primarily from physical effects such as restricted polymer mobility at the particle–polymer interface.

Although the curing of preceramic polymers and the densification benefits of ceramic fillers have each been studied individually, no prior work has systematically linked filler particle size to the curing kinetics, reaction mechanism, and activation thermodynamics of SMP-10. Earlier studies on SMP-10 and related AHPCS precursors have largely reported a single overall activation energy or qualitative shifts in curing temperature, without resolving how the controlling mechanism evolves with conversion. Studies on ceramic-filled preceramic polymers have focused predominantly on shrinkage reduction, packing, and densification during pyrolysis rather than on the curing step itself, while the broader thermoset-nanocomposite literature has demonstrated filler-size effects on cure kinetics in organic resins that have not been transferred to silicon-based preceramic systems. The novelty of the present work lies in

directly comparing micro- and nano-sized SiC at matched loadings within the same precursor and combining model-free isoconversional kinetics, master plot mechanism identification, and transition-state thermodynamic analysis. This integrated approach distinguishes physical (heat-transfer and interfacial-mobility) effects from intrinsic curing chemistry and provides a quantitative basis for selecting filler size and loading to tailor cure schedules in PIP-derived SiC-matrix composites.

The objective of this study is therefore to investigate the influence of SiC particle size and loading on the curing kinetics of SMP-10. Differential scanning calorimetry (DSC) was used to analyze the curing behavior of SMP-10 containing micro- and nano-sized SiC particles at different filler concentrations. Kinetic parameters were determined using multiple non-isothermal methods, including Kissinger, Ozawa, FWO, KAS, and Starink. In addition, master-plot analysis and transition-state thermodynamic parameters (ΔH, ΔS, and ΔG) were used to interpret the physical origin of the rate-controlling step.

2 Methodology

2.1 Materials and Instruments

Allylhydridopolycarbosilane (StarPCS^{TM} SMP-10) with a viscosity of 40–100 cP at 25 °C and a density of 0.998 g·cm^{-3}, used as the silicon carbide matrix precursor, was obtained from Starfire Chemicals (USA). β-SiC powder with an average particle size of 1 µm (99 %) was purchased from Beantown Chemicals. Nano-sized β-SiC particles of 40 nm were obtained from SkySpring Nanomaterials, Inc. Acetone (99.5 %) was supplied by VWR Chemicals. High-purity nitrogen gas (99.999%, Redball Oxygen) was used to maintain an inert atmosphere during the differential scanning calorimetry (DSC).

2.2 Sample Preparation

The SMP-10 preceramic polymer was preheated at 110 °C in a vacuum oven (MTI Corporation, model DZF-6020-HT400) to remove low-molecular-weight oligomers, thereby promoting cross-linking and improving the ceramic yield[4]. The preheated SMP-10 was then used to prepare slurries containing either micro-sized or nano-sized SiC fillers. The required amount of SiC filler was directly added to the SMP-10 precursor without the use of dispersing agents or solvents. The micro-SiC slurries were mechanically stirred at room temperature for 30 to 40 minutes until a visually homogeneous mixture was obtained. For the nano-SiC slurries, which are more prone to agglomeration, a planetary mixer (FlackTek Inc. Speedmixer,DAC 150.1 FVZ-K, operated at 3000 rpm for 2 minutes) was used to improve dispersion and break up agglomerates. The fillers were added to SMP-10 at weight ratios of 0.1 : 0.9, 0.2 : 0.8, and 0.3 : 0.7 (SiC : SMP-10). Two sets of slurries were therefore prepared, one incorporating micro-SiC and the other nano-SiC, to enable a comparative study of the effect of filler size on the curing behavior of SMP-10. It should be noted that a detailed characterization of the particle dispersion and agglomeration state was not performed in this study; the possible influence of residual agglomeration on the effective interfacial area represents a limitation and a subject for future investigation. All samples were subjected to differential scanning calorimetry (DSC) to analyze the curing reactions.

2.3 Thermo-chemical characterization of preceramic polymer

Differential Scanning Calorimetry Analysis

Differential Scanning Calorimetry (DSC) (TA instruments DSC2500; Tzero hermetic aluminum pans) was employed to investigate the thermal behavior of the samples by monitoring both physical and chemical transitions under controlled temperature conditions. The experiments were performed over a temperature range of 50 to 400 °C at heating rates of 0.5, 1, 2.5, 5, and 10 °C min^{-1}. Sample masses were maintained at approximately 20 ± 2 mg. The analyzed compositions consisted of SMP-10 containing silicon carbide fillers at weight ratios of 0.1 SiC : 0.9 SMP-10, 0.2 SiC : 0.8 SMP-10, and 0.3 SiC : 0.7 SMP-10. For each composition, either micro-sized or nano-sized SiC particles were employed, resulting in a total of six distinct sample formulations. DSC measurements at selected heating rates were repeated to evaluate experimental reproducibility. The repeated runs reproduced the peak curing temperature to within approximately 2.5 °C on average. The reliability of the extracted kinetic parameters is further supported

by the high linearity of the isoconversional fits ($R^2 > 0.96$) and by the close agreement among the KAS, FWO, and Starink methods. Comparable sample masses and identical experimental conditions were used in all experiments to ensure consistent thermal histories and reliable comparison across heating rates and sample compositions. The DSC heat flow data were baseline corrected and integrated in OriginPro. For each thermogram, the onset and end of the curing exotherm were defined manually as the temperatures at which the heat flow signal departed from and returned to the baseline, and these points were used as the limits of integration. A linear baseline connecting these two points was subtracted, and the conversion was obtained by integrating the baseline-corrected heat flow between these limits, normalized to the total reaction enthalpy. The same baseline correction and integration criteria were applied consistently to all formulations and heating rates.

3 Theory

Thermal analysis techniques such as differential scanning calorimetry (DSC) provide valuable tools for studying curing reactions in preceramic polymers. Non-isothermal kinetic analysis using multiple heating rates allows the determination of activation energies and reaction mechanisms without assuming a specific kinetic model. Methods such as Kissinger, Ozawa, Flynn–Wall–Ozawa (FWO), Kissinger–Akahira–Sunose (KAS), and Starink analyses are commonly employed to determine apparent activation energies as a function of conversion. When combined with master-plot analysis and transition-state thermodynamics, these methods provide deeper insight into the nature of the rate-controlling step and the energetic landscape of the curing reaction.[33,34]. A comprehensive theoretical description of the kinetic framework and analysis procedures has been reported previously[23]; therefore, only the essential equations and definitions relevant to the present work are summarized here.

Kissinger and Ozawa

Peak-based methods were employed to obtain an initial estimate of the apparent activation energy from the shift in the temperature of maximum reaction rate, $T_{\max}$, observed in DSC curves recorded at different heating rates, β.

The Kissinger method[35] is expressed as:

$$\log\left(\frac{\beta}{T_{\max}^2}\right) = \log\left(\frac{ZR}{E_a}\right) - \frac{E_a}{2.303RT_{\max}} \tag{1}$$

The Ozawa method[36] is given by:

$$\log\beta = \log\left(\frac{ZE_a}{R}\right) - 2.315 - 0.4567\left(\frac{E_a}{RT_{\max}}\right) \tag{2}$$

where β is the heating rate ($\mathrm{K\,min^{-1}}$), $T_{\max}$ is the temperature corresponding to the maximum reaction rate obtained from the DSC exothermic peak (K), E_a is the apparent activation energy ($\mathrm{kJ\,mol^{-1}}$), Z is the pre-exponential factor ($\mathrm{min^{-1}}$), and R is the universal gas constant ($8.314\ \mathrm{J\,mol^{-1}\,K^{-1}}$).

Peak-based methods such as the Kissinger and Ozawa approaches are commonly used to obtain an initial estimate of the apparent activation energy under non-isothermal conditions. These methods rely on the shift of the peak reaction temperature with heating rate. In both cases, the activation energy was obtained from the slope of the corresponding linear plots.

3.1 Model-Free Isoconversional Analysis

To account for conversion-dependent kinetics, model-free isoconversional analysis was performed by evaluating reaction behavior at fixed extents of conversion, α, across multiple heating rates[37–39]. The general kinetic expression is:

$$\frac{d\alpha}{dt} = A \exp\left(-\frac{E_a}{RT}\right) f(\alpha) \tag{3}$$

The extent of conversion was calculated from DSC heat flow curves as:

$$\alpha(T) = \frac{\int_{T_0}^{T} \dot{q}(T')\, dT'}{Q_{\text{total}}} \tag{4}$$

where $\dot{q}(T)$ is the heat flow signal and Q_{total} is the total reaction enthalpy.

Kissinger–Akahira–Sunose (KAS)

The KAS method[40] was applied according to:

$$\ln\left(\frac{\beta}{T^2}\right) = \ln\left(\frac{ZR}{E_a f(\alpha)}\right) - \frac{E_a}{RT} \tag{5}$$

Activation energy was determined from the slope of $\ln(\beta/T^2)$ versus $1/T$ at fixed α.

Flynn–Wall–Ozawa (FWO)

The FWO method[41] is expressed as:

$$\ln\beta = \ln\left(\frac{ZE_a}{Rf(\alpha)}\right) - 5.331 - 1.052\left(\frac{E_a}{RT}\right) \tag{6}$$

Starink

The Starink method[42] was applied as:

$$\ln\left(\frac{\beta}{T^{1.92}}\right) = \text{const.} - 1.0008\left(\frac{E_a}{RT}\right) \tag{7}$$

Parallel application of KAS, FWO, and Starink methods enabled cross-validation of activation energy behavior.

Thermodynamic Parameters

The thermodynamic parameters associated with the activated complex were evaluated within the framework of transition state theory using kinetic parameters obtained from isoconversional analysis. All thermodynamic parameters were calculated at temperatures corresponding to a fixed degree of conversion, T_α, thereby ensuring a consistent representation of the reaction progress during the curing process.

The enthalpy of activation ($\Delta H^{\ddagger}$), entropy of activation ($\Delta S^{\ddagger}$), and Gibbs free energy of activation ($\Delta G^{\ddagger}$) were determined using the following relationships[43]:

$$\Delta H^{\ddagger} = E_a - RT_\alpha \tag{8}$$

$$\Delta S^{\ddagger} = R \ln\left(\frac{Z\,h}{k_{\mathrm{B}}\,T_{\alpha}}\right) \tag{9}$$

$$\Delta G^{\ddagger} = \Delta H^{\ddagger} - T_{\alpha}\,\Delta S^{\ddagger} \tag{10}$$

In these expressions, E_a denotes the activation energy, Z is the pre-exponential factor obtained from the KAS method, R is the universal gas constant, k_{B} is the Boltzmann constant ($1.381 \times 10^{-23}\ \mathrm{J\,K^{-1}}$), h is the Planck constant ($6.626 \times 10^{-34}\ \mathrm{J\,s}$), and T_{α} represents the temperature corresponding to a given extent of conversion.

The pre-exponential factor Z represents an effective kinetic parameter derived from the isoconversional analysis. Accordingly, the entropy and Gibbs free energy of activation calculated using this approach are employed primarily for comparative assessment of curing behavior rather than as absolute thermodynamic quantities.

The KAS method permits direct estimation of the pre-exponential factor and is therefore suitable for evaluating transition state thermodynamic parameters. In contrast, although the FWO and Starink methods yield reliable activation energy values, they do not enable determination of Z, which precludes calculation of $\Delta S^{\ddagger}$ and $\Delta G^{\ddagger}$ within the framework of transition state theory. This treatment follows established procedures reported in the literature[43].

3.2 Reaction Mechanism Determination (Master Plot Method)

Once the activation energy behavior was established through isoconversional analysis, the dominant reaction mechanism was investigated using the master plot method[39]. This approach enables the identification of the kinetic model function $f(\alpha)$ that best describes the rate-controlling step of the solid-state reaction by comparing experimental data with theoretical model curves[44].

In solid-state kinetics, several reaction mechanisms may describe the transformation process. These mechanisms are commonly classified into four main categories[45]:

- **Reaction-order models (Fn)**, in which the reaction rate depends on the unreacted fraction, typically expressed as $(1-\alpha)^n$. These empirical models are often used to describe simple decomposition or curing reactions (e.g., F1, F2, F3).
- **Geometrical contraction models (Rn)**, which assume that the reaction progresses inward from the surface of particles at a constant rate. The geometry (planar, cylindrical, or spherical) determines the mathematical form of $f(\alpha)$ (e.g., R3 for a contracting sphere).
- **Diffusion-controlled models (Dn)**, where the reaction rate is limited by the diffusion of species through a growing product layer. Typical examples include the Jander (D3) and Ginstling–Brounshtein (D4) models.
- **Nucleation and growth models (An)**, such as the Avrami–Erofeev models, which describe processes involving the formation of stable nuclei followed by their growth. These models are commonly applied to polymeric reactions and crystallization phenomena (e.g., A2, A3).

Master plot

The master plot analysis was carried out using normalized experimental kinetic curves and theoretical model functions. For all samples, the conversion–temperature data obtained at different heating rates were first processed to ensure a unique conversion value for each temperature. In cases where multiple conversion values corresponded to the same temperature, the median value was retained.

For the 0.1, 0.2, and 0.3 micro-SiC samples as well as the 0.1 and 0.3 nano-SiC samples, the experimental master plots were constructed using the full conversion-dependent activation energy $E_a(\alpha)$ obtained from the KAS isoconversional method. In contrast, for the 0.2 nano-SiC sample, the activation energy exhibited a larger variation with conversion. To avoid numerical instabilities associated with the direct use of strongly varying $E_a(\alpha)$ in the master plot construction, a single representative activation energy value corresponding to $\alpha = 0.5$ was employed. This approach is commonly adopted in master plot analyses when a characteristic activation energy is required for normalization[46,47].

To obtain a stable and physically meaningful reaction rate, the experimental $\alpha(T)$ curves were smoothed using cubic spline interpolation. The derivative $d\alpha/dT$ was calculated analytically from the spline function, which avoids numerical instabilities associated with direct finite-difference differentiation.

The experimental master plot was calculated according to:

$$MP(\alpha) = \frac{d\alpha}{dT} \exp\left(\frac{E_a}{RT}\right)$$

where R is the gas constant, T is the temperature corresponding to a given conversion level, and E_a represents either the conversion-dependent or representative activation energy, as described above.

Each experimental master plot was normalized to its value at $\alpha = 0.5$, yielding the dimensionless function $f(\alpha)/f(0.5)$. This normalization removes rate-dependent prefactors and allows direct comparison between data obtained at different heating rates. The final experimental master plot was obtained by averaging the normalized curves from all heating rates, while the corresponding standard deviation was used to assess data dispersion.

Comparison with theoretical models

The experimental master plots were compared with theoretical master plots derived from the kinetic models listed above. All theoretical functions were normalized in the same manner as the experimental data. The agreement between experimental and theoretical master plots was quantified using the root mean square error (RMSE) over the selected conversion range. The kinetic model with the lowest RMSE was considered to best represent the dominant reaction mechanism for each sample.

4 Results and Discussion

4.1 Thermal Curing Profiles

The non-isothermal curing behavior of SMP-10 containing different loadings of micro sized SiC particles (0.1, 0.2, and 0.3 SiC : SMP-10 mass ratios) was investigated by DSC at heating rates ranging from 0.5 to 10 °C min^{-1}. The corresponding DSC thermograms and conversion–temperature curves are shown in Figures 1, 2, and 3 for the different filler contents.

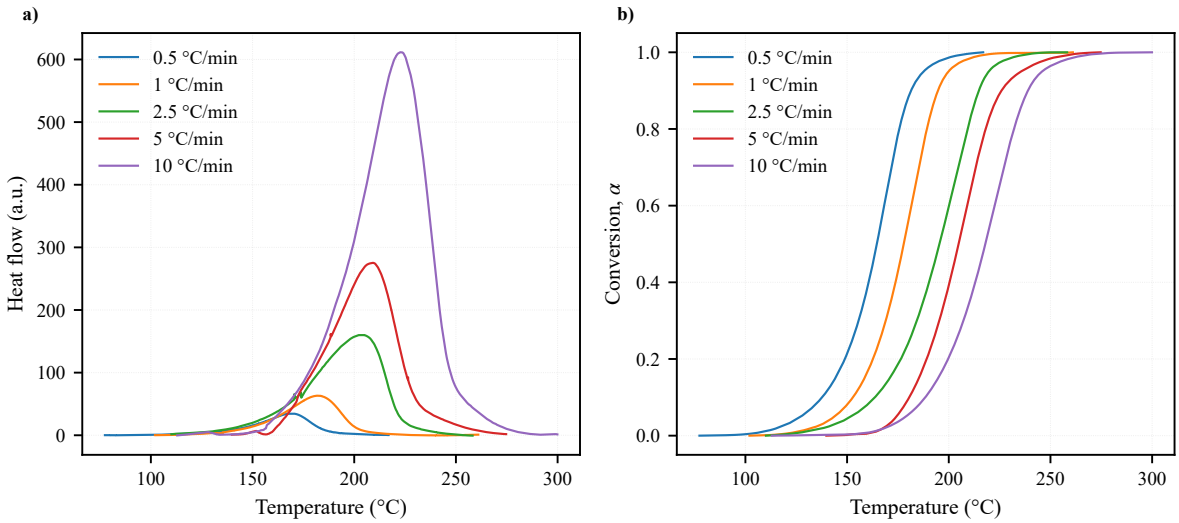

Fig. 1: *DSC thermograms (a) and conversion curves (b) for SMP-10 with 0.1 micro SiC.*

For all micro-SiC-containing compositions, the DSC thermograms exhibit a single dominant exothermic peak, indicating that SMP-10[23] curing proceeds through an overall crosslinking reaction involving hydrosilylation, dehydrocoupling characteristic of allylhydridopolycarbosilane systems. As the heating rate increases, the exothermic peak shifts systematically toward higher temperatures, reflecting the kinetically controlled nature of the curing process under non-isothermal conditions. At lower heating rates, broader and less intense peaks are observed, suggesting that polymer chains have sufficient time to rearrange and react over an extended temperature range. In contrast, higher heating rates result in sharper and more intense peaks, as higher temperatures are required to achieve comparable reaction rates within shorter time scales (Figures 1a–3a). This shift reflects the kinetic nature of the curing process, where higher heating rates reduce the time available for reaction at each temperature, requiring higher temperatures to reach equivalent reaction rates.

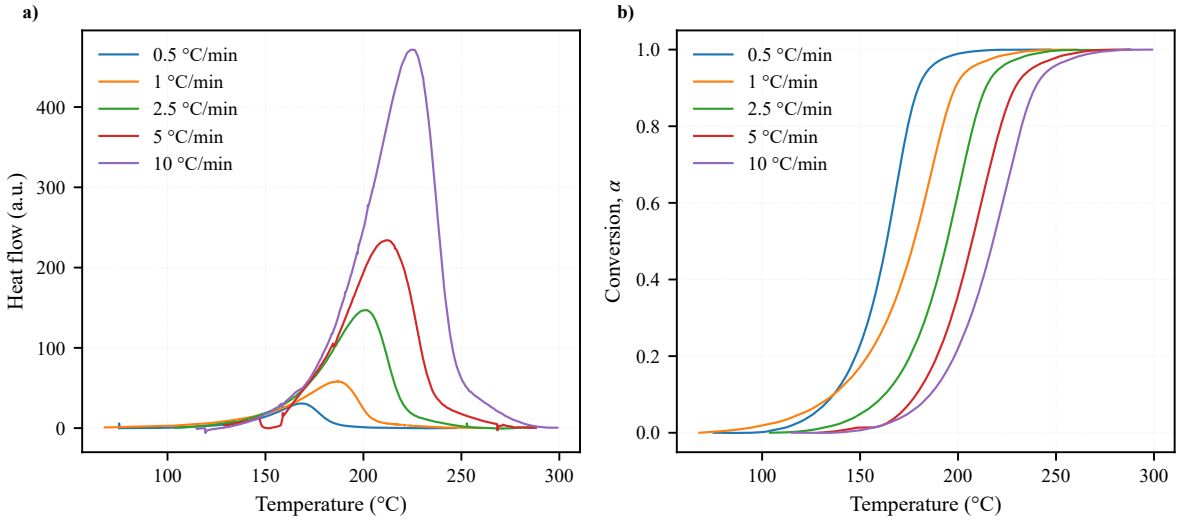

Fig. 2: *DSC thermograms (a) and conversion curves (b) for SMP-10 with 0.2 micro SiC.*

The corresponding conversion–temperature curves derived from the DSC data display sigmoidal profiles for all micro-SiC loadings, with conversion progressing gradually at low temperatures, followed by a rapid increase at intermediate temperatures and a gradual approach to full conversion of $\alpha \rightarrow 1$ by temperature of 300 °C for all compositions. For a given heating rate, increasing the micro-SiC content from 0.1 to 0.3 results in a modest shift of the conversion curves toward higher temperatures, indicating a slight delay in the onset and progression of curing (Figures 1b–3b). This slight delay in the curing process is due to the dilution of the reactive polymer phase and reduced effective concentration of crosslinkable functional groups. Despite these changes, complete conversion is achieved for all micro-SiC-filled systems within the investigated temperature range.

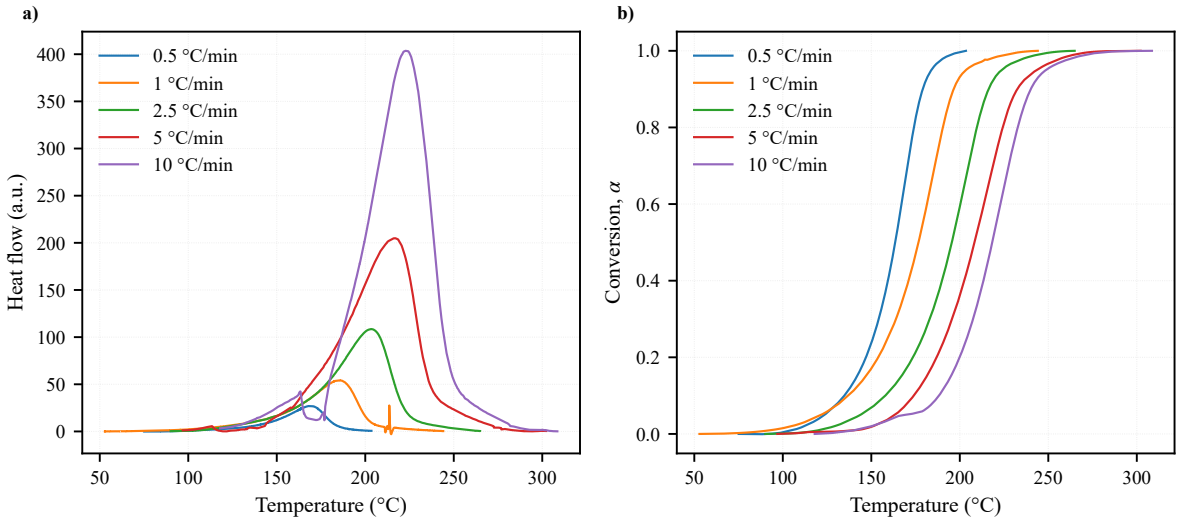

Fig. 3: *DSC thermograms (a) and conversion curves (b) for SMP-10 with 0.3 micro SiC.*

The curing behavior of SMP-10 systems containing nano-sized SiC particles exhibits similar qualitative trends with respect to heating rate, as shown by the DSC thermograms in Figures 4a–6a. For all nano-SiC loadings, the curing exotherms shift toward higher temperatures with increasing heating rate, confirming the kinetically controlled nature of the curing process under non-isothermal conditions. Compared to the micro-SiC-filled systems, the nano-SiC-containing samples show a greater shift of the exothermic peaks toward higher temperatures at comparable filler loadings. Nano-SiC particles provide a significantly larger surface area, increasing polymer–particle interfacial interactions. These interactions can restrict segmental mobility of the polymer chains near the particle surface, increasing the effective energy required for network formation [48].

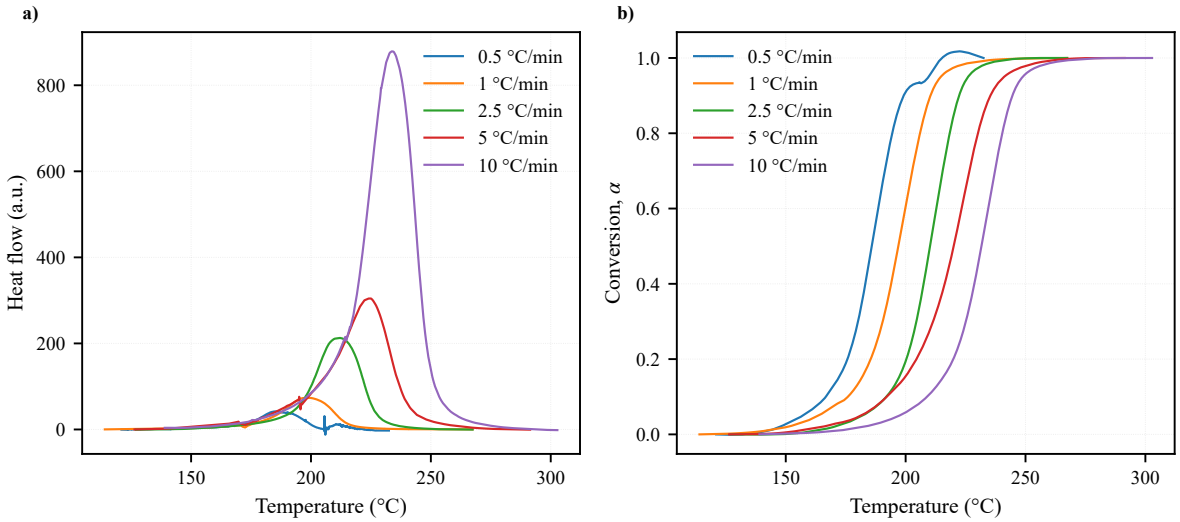

Fig. 4: *DSC thermograms (a) and conversion curves (b) for SMP-10 with 0.1 nano SiC.*

The conversion–temperature curves for the nano-SiC-filled systems also retain a sigmoidal shape, but the onset and progression of conversion occur at higher temperatures compared to the micro-SiC-filled counterparts. With increasing nano-SiC content, the conversion curves shift progressively toward higher temperatures and become steeper at intermediate conversion levels (Figures 4b–6b). Nevertheless, full conversion is achieved for all nano-SiC loadings

and heating rates investigated.

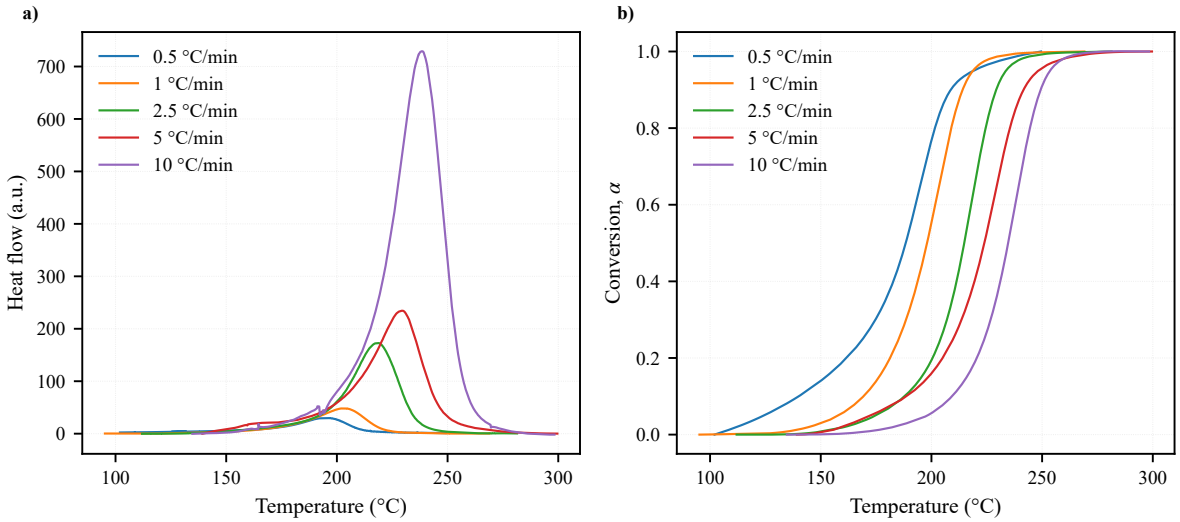

Fig. 5: *DSC thermograms (a) and conversion curves (b) for SMP-10 with 0.2 nano SiC.*

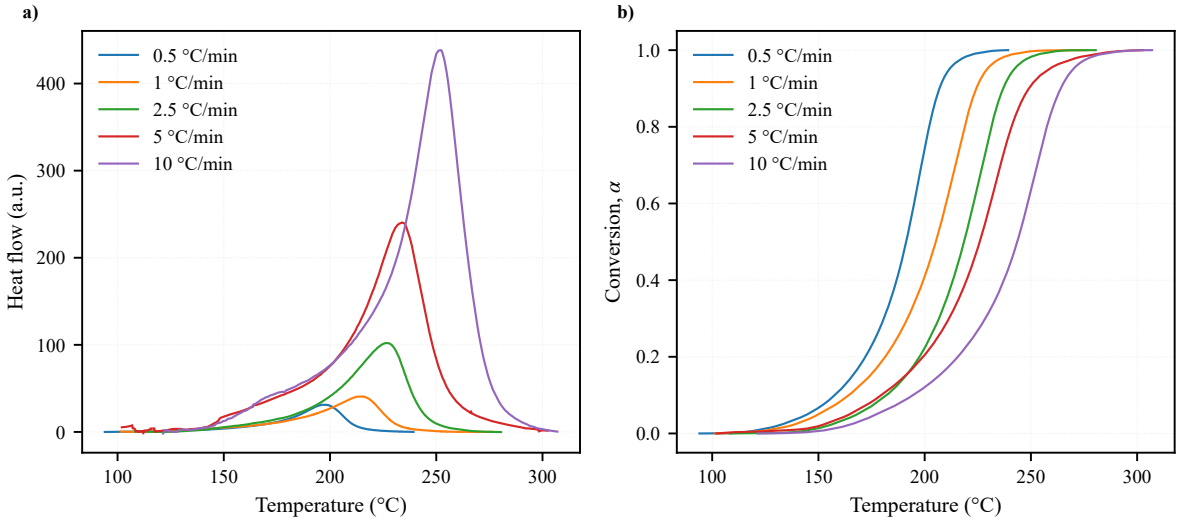

Fig. 6: *DSC thermograms (a) and conversion curves (b) for SMP-10 with 0.3 nano SiC.*

To enable a direct comparison between unfilled and particle-filled systems, the DSC thermograms for pure SMP-10 and SMP-10 containing micro- and nano-sized SiC particles at different loadings are overlaid in Figure 7. The pure SMP-10 system exhibits a curing exotherm centered at an intermediate temperature, serving as a reference for assessing the influence of particulate addition. Upon incorporation of micro-sized SiC particles, the curing exotherms shift moderately toward higher temperatures with increasing filler content, accompanied by a reduction in peak heat flow, consistent with dilution of the reactive polymer fraction.

In contrast, incorporating nano-sized SiC shifts the curing exotherms toward higher temperatures at comparable filler loadings, consistent with delayed conversion progress in the corresponding $\alpha(T)$ curves (Figures 4–6). At equivalent particle contents, the nano-SiC-filled systems also exhibit narrower and more sharply defined exothermic peaks relative to both the pure polymer and the micro-SiC-filled systems. The narrower peaks suggest a more

localized curing event occurring over a narrower temperature range, consistent with delayed initiation followed by rapid crosslinking once sufficient thermal energy overcomes interfacial mobility constraints[49].

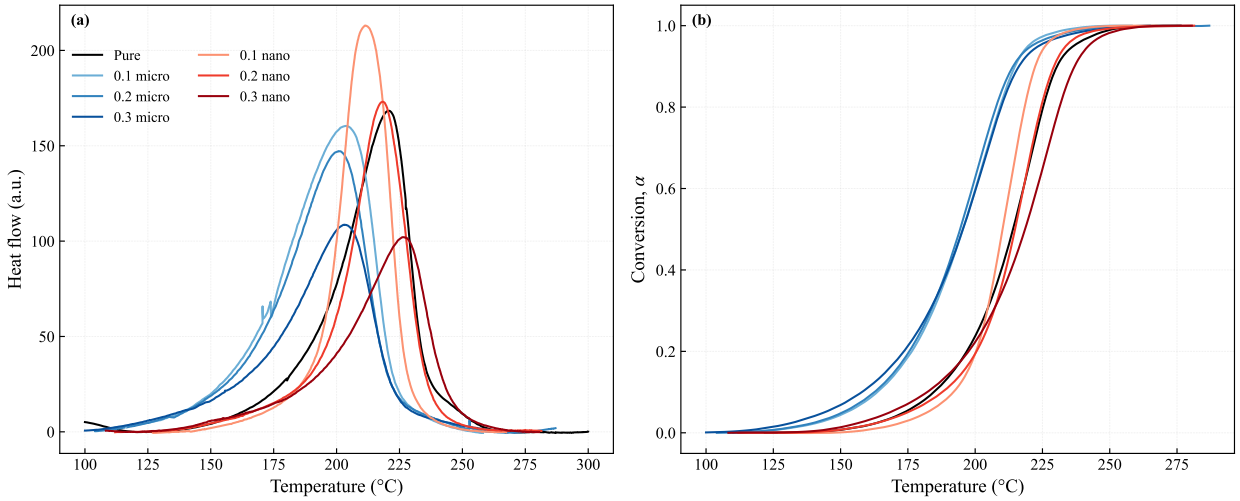

Fig. 7: *(a) DSC thermograms and (b) conversion (α) versus temperature for SMP-10 with and without nano and micro particles at a representative heating rate of 2.5 °C min^{-1}.*

The higher curing temperatures observed for the nano-SiC-filled systems relative to both the pure SMP-10 and the micro-SiC-filled systems are attributed to physical effects associated with particle size rather than changes in the intrinsic curing chemistry. Nano-sized SiC particles create a larger polymer–particle interfacial area, which strengthens polymer–particle interactions and limits polymer chain mobility. Consequently, greater thermal energy is required to facilitate the molecular rearrangements necessary for effective crosslinking, resulting in a shift of the curing exotherms toward higher temperatures, as observed in Figure 7. Although the nano-SiC slurries were prepared using a planetary mixer to limit agglomeration, residual agglomeration cannot be entirely excluded and may contribute as a secondary factor to the delayed curing exotherms and the stronger conversion dependence observed for the nano-filled systems. Nevertheless, the systematic and monotonic shift of the curing exotherms with increasing nano-SiC content is consistent with a dominant contribution from the increasing polymer–particle interfacial area rather than from irregular agglomeration effects.

The effect can be seen from the peak curing temperatures measured at a representative heating rate of 2.5 °C min^{-1}. For the micro-SiC-filled systems, the peak temperatures remain lower than that of pure SMP-10, with values of 202.7 °C, 200.8 °C, and 203.4 °C for micro-SiC contents of 0.1, 0.2, and 0.3. In contrast, the nano-SiC-filled systems show higher peak temperatures under the same heating conditions, increasing from 211.3 °C at 0.1 nano-SiC to 218.1 °C and 226.1 °C at 0.2 and 0.3. This difference of approximately 10–20 °C demonstrates that nanoparticle addition has a stronger influence on curing kinetics than micro-sized fillers. The corresponding conversion–temperature curves at 2.5 °C min^{-1} are shown in Figure 7b. Consistent with the peak-temperature trend, the micro-SiC systems reach a given conversion at temperatures close to pure SMP-10, whereas the nano-SiC systems require progressively higher temperatures with increasing loading, reflecting the restricted chain mobility induced by the larger interfacial area.

This difference is also reflected in the conversion–temperature behavior. In comparison, micro-sized SiC particles act mainly as inert volume fillers that reduce the fraction of reactive polymer and have a smaller influence on polymer chain mobility. As a result, the curing exotherms of the micro-SiC-filled systems shift less than those of the nano-SiC-filled systems under identical heating conditions. For the nano-SiC-filled systems, the same degree of conversion is reached at higher temperatures than for pure SMP-10 and the micro-SiC-filled systems. The larger polymer–particle interfacial area in the nano-filled compositions limits polymer chain mobility and slows the curing process, shifting the conversion curves toward higher temperatures.

4.2 Kinetic Analysis

Peak-based kinetic analysis was first used to obtain an initial estimate of the apparent activation energy for SMP-10 systems containing micro- and nano-sized SiC fillers. The activation energies obtained from the Kissinger and Ozawa methods are summarized in Table 1. For all investigated systems, the two methods give comparable values and high linear correlation coefficients ($R^2 > 0.96$), indicating good linearity of the peak-based plots and confirming the statistical reliability of the extracted kinetic parameters.

Table 1: *Activation energies and pre-exponential factors obtained from Kissinger and Ozawa analyses.*

System	Method	E_a [kJ mol^{-1}]	Z [min^{-1}]	R^2
SMP-10 Pure	Kissinger	109.3 ± 5.8	5.4×10^{10}	0.992
	Ozawa	111.6 ± 5.6	1.1×10^{11}	0.993
SMP-10 + 0.1 micro SiC	Kissinger	93.5 ± 7.5	2.9×10^{9}	0.974
	Ozawa	96.3 ± 7.2	7.5×10^{9}	0.977
SMP-10 + 0.2 micro SiC	Kissinger	91.5 ± 6.0	1.6×10^{9}	0.982
	Ozawa	94.4 ± 5.8	4.4×10^{9}	0.986
SMP-10 + 0.3 micro SiC	Kissinger	88.2 ± 7.9	6.5×10^{8}	0.969
	Ozawa	91.3 ± 7.5	1.9×10^{9}	0.973
SMP-10 + 0.1 nano SiC	Kissinger	107.3 ± 3.0	2.0×10^{11}	0.997
	Ozawa	114.9 ± 3.0	3.9×10^{11}	0.997
SMP-10 + 0.2 nano SiC	Kissinger	117.2 ± 3.8	2.0×10^{12}	0.996
	Ozawa	125.0 ± 3.9	3.4×10^{12}	0.996
SMP-10 + 0.3 nano SiC	Kissinger	107.1 ± 9.8	8.2×10^{10}	0.968
	Ozawa	114.9 ± 9.8	1.7×10^{11}	0.972

The apparent activation energies obtained from the Kissinger and Ozawa analyses reveal a systematic dependence on both filler size and filler loading in Table 1. For the micro-SiC-filled systems, the average activation energy decreases relative to pure SMP-10[23] and shows a gradual reduction with increasing particle content. The decrease in apparent activation energy likely arises from heterogeneous effects introduced by the filler particles. Micro-SiC surfaces may facilitate localized polymer rearrangements or act as heterogeneous sites that promote crosslinking reactions, thereby lowering the effective energy barrier for network formation[50]. The reduction in apparent activation energy is unlikely to originate from a single cause. Several physical effects can contribute. Silicon carbide has a high intrinsic thermal conductivity, so the more conductive filled samples experience improved heat transfer and reduced thermal lag, which lowers the apparent peak temperature and the apparent activation energy. A comparable behaviour has been reported for thermally conductive SiC added to rubber compounds, where the curing exotherm shifted to lower temperatures and the apparent activation energy decreased as the heat transfer into the material improved. Dilution of the reactive polymer fraction also occurs, although this effect is expected to slow the reaction and account for the modest delay in conversion rather than for the decrease in activation energy. A local surface contribution at the particle interface cannot be excluded, but the master plot analysis shows the same nucleation and growth mechanism as in unfilled SMP-10, which argues against a change in the intrinsic curing chemistry. The present measurements do not allow these contributions to be separated, so the lower apparent activation energy is best understood as the combined outcome of physical effects, dominated by enhanced heat transfer, rather than as evidence of altered curing chemistry. This interpretation is consistent with the near constant Gibbs free energy of activation across all formulations, which indicates that the filler redistributes the enthalpic and entropic contributions rather than changing the thermodynamic feasibility of network formation.

In contrast, the nano-SiC-filled systems exhibit activation energies that are comparable to or higher than those of the pure polymer, with a general tendency to increase as the nano-particle loading increases. The increase reflects stronger polymer–particle interfacial interactions. The large surface area of nanoscale fillers creates an interphase region in which polymer segmental mobility is reduced, requiring greater thermal energy for the molecular rearrangements necessary for crosslinking. Consistent with these kinetic trends, the nano-filled systems require higher temperatures to

reach comparable reaction rates under non-isothermal conditions, which aligns with the systematic right-shift of the DSC curing exotherms observed in Figure 7.

Isoconversional Analysis of Activation Energy

While the Kissinger and Ozawa peak-based methods yield a single apparent activation energy, they do not account for possible variations of activation energy during the curing process. To evaluate the evolution of the activation energy with the degree of conversion and assess how particle size influences the curing behavior, model-free isoconversional analysis was performed using the KAS, FWO, and Starink methods. Figures 8 a–10 a present the evolution of the apparent activation energy as a function of conversion for SMP-10 containing 0.1, 0.2, and 0.3 micro-SiC particles, respectively. For all micro-filled compositions, the activation energy exhibits a smooth and relatively weak dependence on conversion, with similar trends obtained from the KAS, FWO, and Starink methods. The near-parallel isoconversional plots over the main conversion range (typically α = 0.2–0.9) indicate that the curing process proceeds through a single dominant reaction mechanism, similar to that of pure SMP-10.

For the micro-SiC-filled systems, Figures 8 b, c, d – 10 b, c, d additionally present the thermodynamic parameters derived from the isoconversional analysis, namely the enthalpy of activation ($\Delta H^{\ddagger}$), entropy of activation ($\Delta S^{\ddagger}$), and Gibbs free energy of activation ($\Delta G^{\ddagger}$). The evolution of $\Delta H^{\ddagger}$ closely follows the trends observed for the apparent activation energy, exhibiting relatively small variations with conversion and progressively lower values with increasing micro-SiC content. This behavior indicates a reduction in the energetic barrier associated with the curing reaction in the presence of micro-sized fillers.

The entropy of activation for the micro-filled systems remains negative over the entire conversion range and becomes increasingly negative with increasing filler loading. The increasingly negative entropy of activation indicates that the transition state becomes more ordered as curing proceeds. This behavior is consistent with the progressive formation of a crosslinked network in which polymer chains lose configurational freedom. Despite these changes in $\Delta H^{\ddagger}$ and $\Delta S^{\ddagger}$, the Gibbs free energy of activation increases smoothly with conversion for all micro-SiC-filled systems. The gradual increase reflects the growing energetic difficulty of network formation as the curing reaction progresses. As crosslink density increases, polymer chain mobility decreases and diffusion of reactive groups becomes more restricted, resulting in a higher effective free-energy barrier for further reaction.[51].

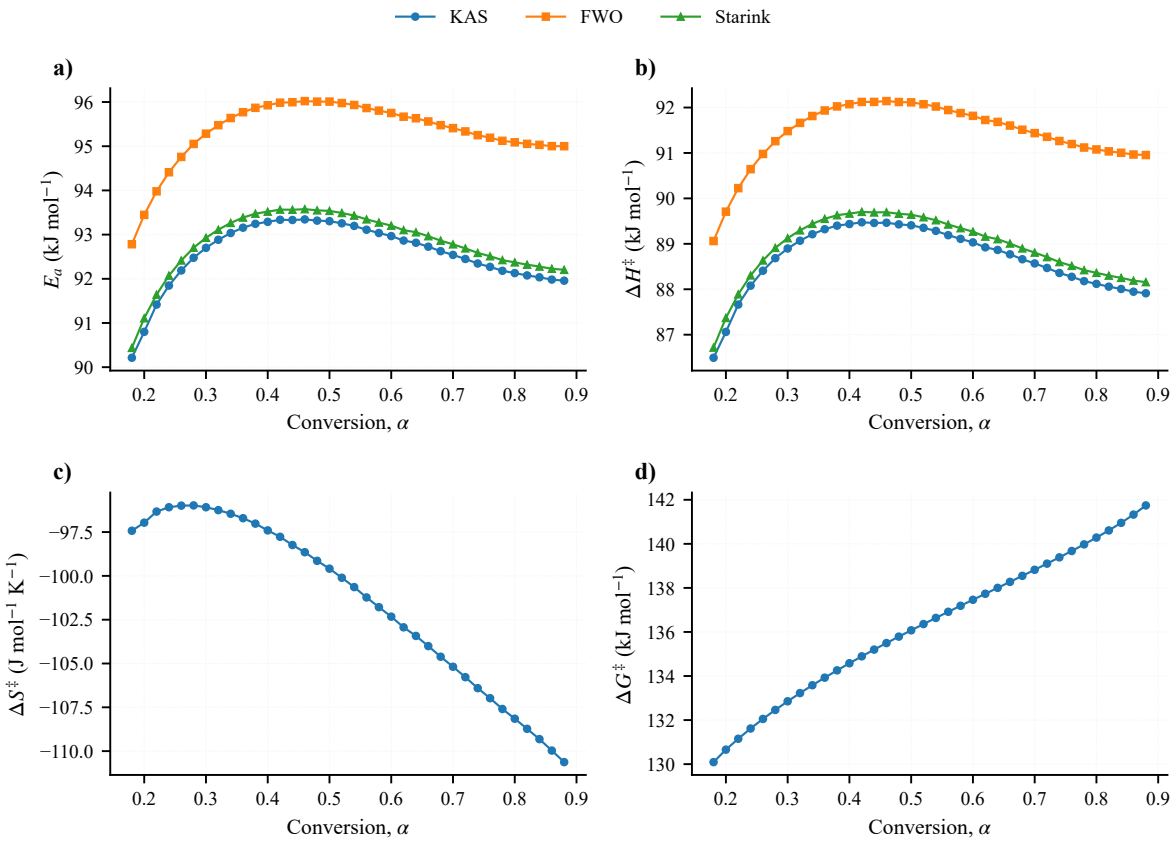

Fig. 8: *Isoconversional kinetic and thermodynamic analysis of SMP-10 with 0.1 micro particles. (a) Activation energy (E_a) as a function of the degree of conversion (α) obtained using the KAS, FWO, and Starink methods. (b) Enthalpy of activation ($\Delta H^{\ddagger}$) calculated from the corresponding E_a values using the temperature T_α derived from the KAS method. (c) Entropy of activation ($\Delta S^{\ddagger}$) determined from the KAS method. (d) Gibbs free energy of activation ($\Delta G^{\ddagger}$) determined from the KAS method.*

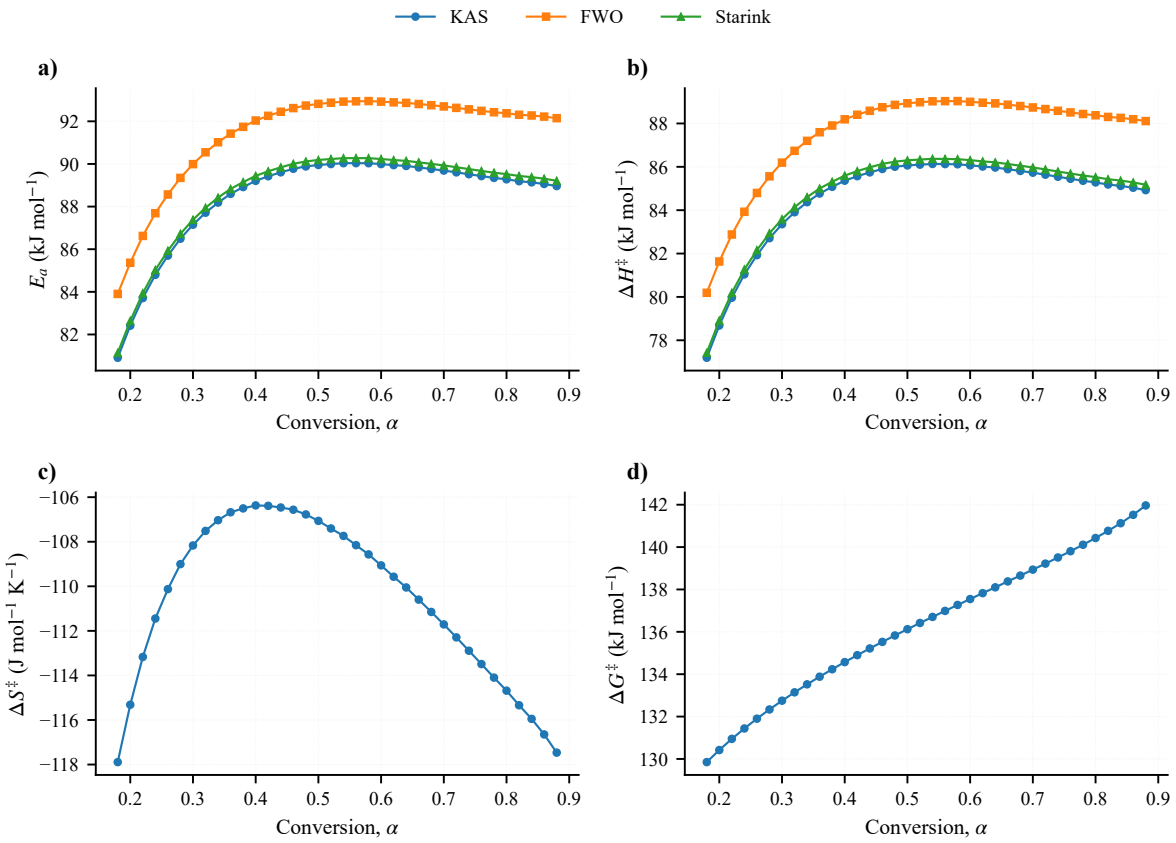

Fig. 9: *Isoconversional kinetic and thermodynamic analysis of SMP-10 with 0.2 micro particles. (a) Activation energy (E_a) as a function of the degree of conversion (α) obtained using the KAS, FWO, and Starink methods. (b) Enthalpy of activation ($\Delta H^{\ddagger}$) calculated from the corresponding E_a values using the temperature T_α derived from the KAS method. (c) Entropy of activation ($\Delta S^{\ddagger}$) determined from the KAS method. (d) Gibbs free energy of activation ($\Delta G^{\ddagger}$) determined from the KAS method.*

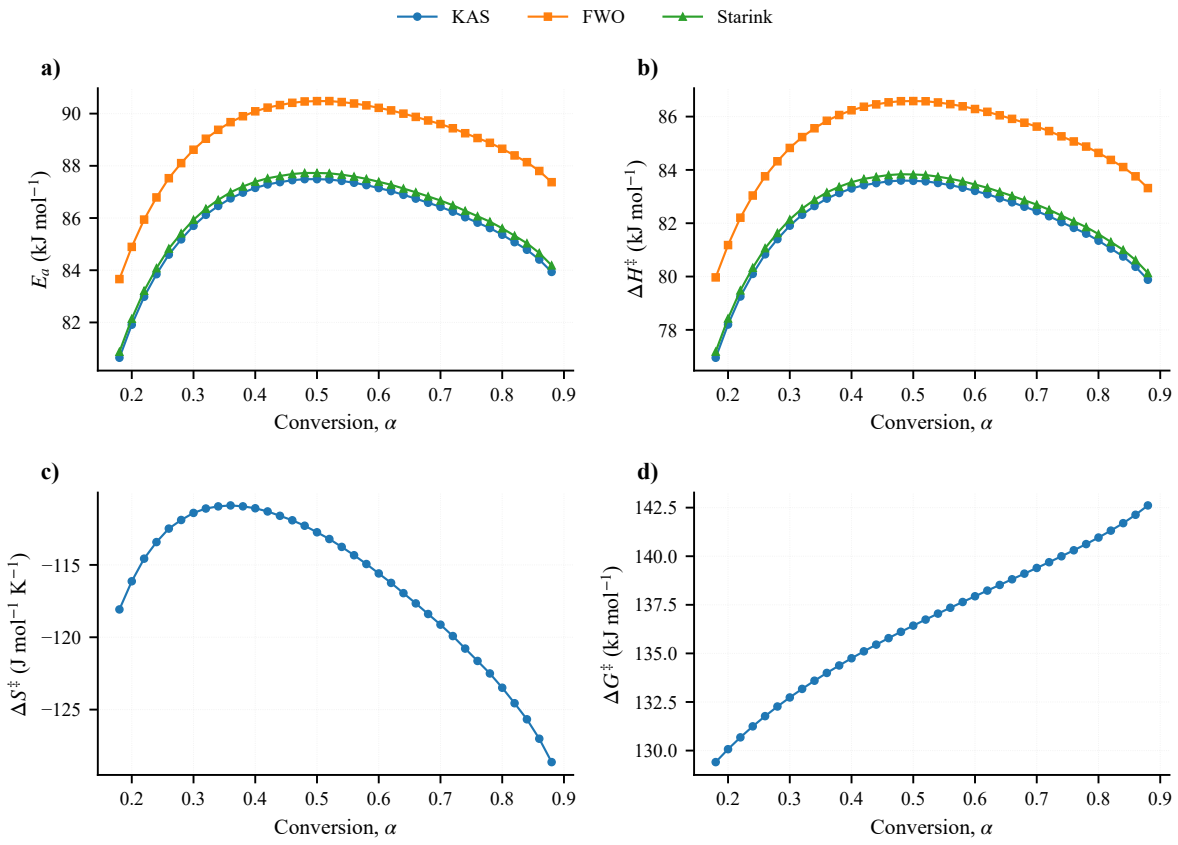

Fig. 10: *Isoconversional kinetic and thermodynamic analysis of SMP-10 with 0.3 micro particles. (a) Activation energy (E_a) as a function of the degree of conversion (α) obtained using the KAS, FWO, and Starink methods. (b) Enthalpy of activation ($\Delta H^{\ddagger}$) calculated from the corresponding E_a values using the temperature T_α derived from the KAS method. (c) Entropy of activation ($\Delta S^{\ddagger}$) determined from the KAS method. (d) Gibbs free energy of activation ($\Delta G^{\ddagger}$) determined from the KAS method.*

Figures 11–13 show the corresponding isoconversional kinetic and thermodynamic parameters for SMP-10 systems containing nano-sized SiC particles at loadings of 0.1, 0.2, and 0.3, respectively. In contrast to the micro-filled systems, the nano-SiC-filled samples exhibit higher apparent activation energies and enthalpies of activation across most of the conversion range, together with a stronger dependence on the degree of conversion. These trends indicate that nano-sized particles have a greater influence on the curing process and suggest that the controlling mechanism evolves during curing likely due to progressive mobility restrictions as the crosslinked network develops in the presence of nanoscale fillers.

For the nano-filled systems, the entropy of activation is less negative at low degrees of conversion but becomes more negative as conversion increases, particularly at higher nano-SiC loadings. Nano-sized fillers limit polymer chain mobility as the crosslinked network develops. In other words, the less negative ΔS‡ at low conversion suggests that early-stage reactions occur primarily in the bulk polymer phase. As curing progresses, however, the growing network interacts more strongly with the nanoparticle surfaces, leading to greater configurational constraints and increasingly negative entropy values[52]. The Gibbs free energy of activation increases with conversion and remains higher than that of the micro-filled systems. This difference arises from the combined energetic and entropic contributions associated with curing in the presence of nano-scale fillers.

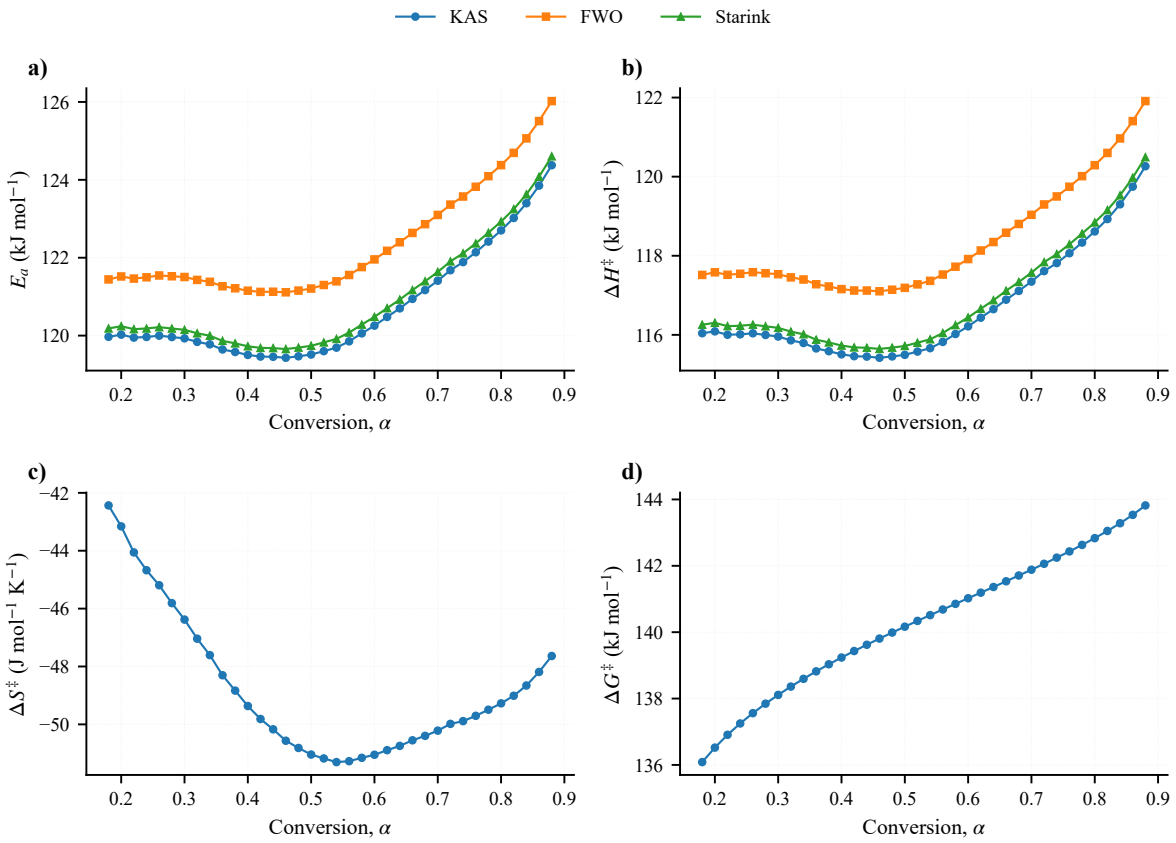

Fig. 11: *Isoconversional kinetic and thermodynamic analysis of SMP-10 with 0.1 nano particles. (a) Activation energy (E_a) as a function of the degree of conversion (α) obtained using the KAS, FWO, and Starink methods. (b) Enthalpy of activation ($\Delta H^{\ddagger}$) calculated from the corresponding E_a values using the temperature T_α derived from the KAS method. (c) Entropy of activation ($\Delta S^{\ddagger}$) determined from the KAS method. (d) Gibbs free energy of activation ($\Delta G^{\ddagger}$) determined from the KAS method.*

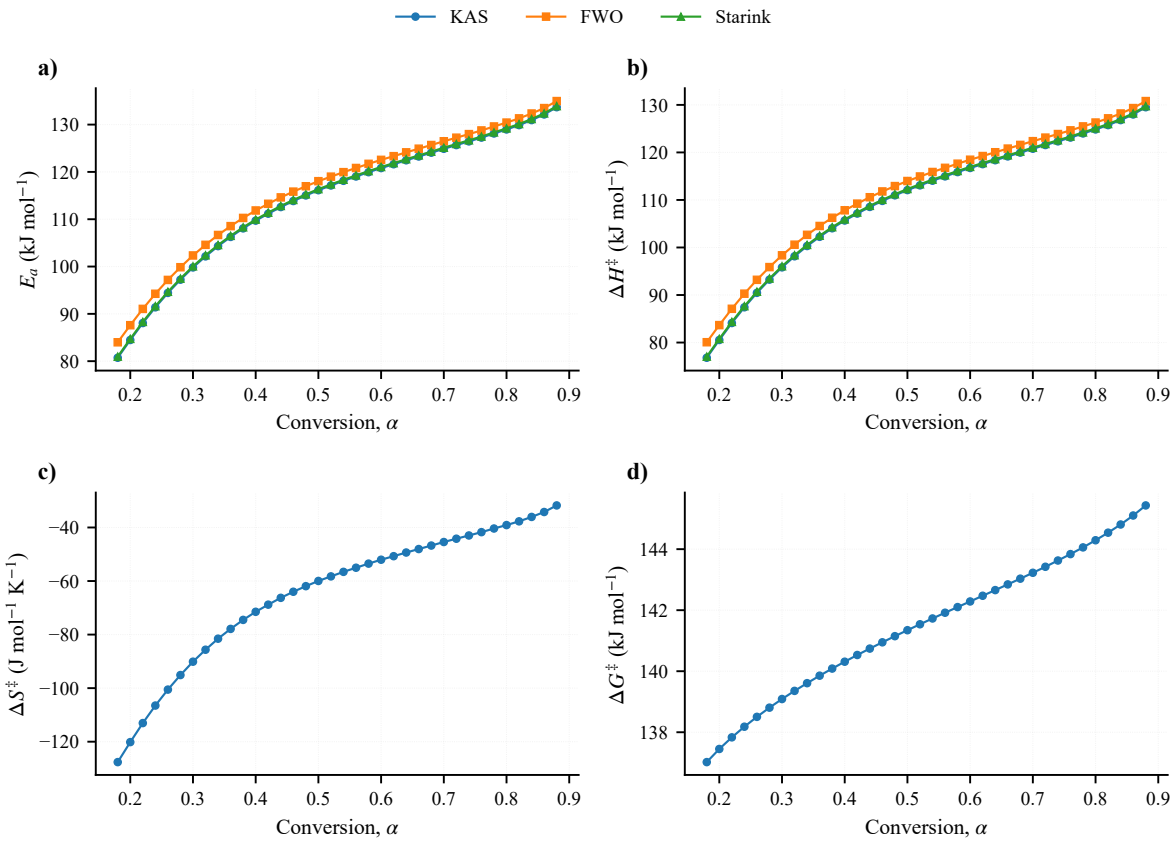

Fig. 12: *Isoconversional kinetic and thermodynamic analysis of SMP-10 with 0.2 nano particles. (a) Activation energy (E_a) as a function of the degree of conversion (α) obtained using the KAS, FWO, and Starink methods. (b) Enthalpy of activation ($\Delta H^{\ddagger}$) calculated from the corresponding E_a values using the temperature T_α derived from the KAS method. (c) Entropy of activation ($\Delta S^{\ddagger}$) determined from the KAS method. (d) Gibbs free energy of activation ($\Delta G^{\ddagger}$) determined from the KAS method.*

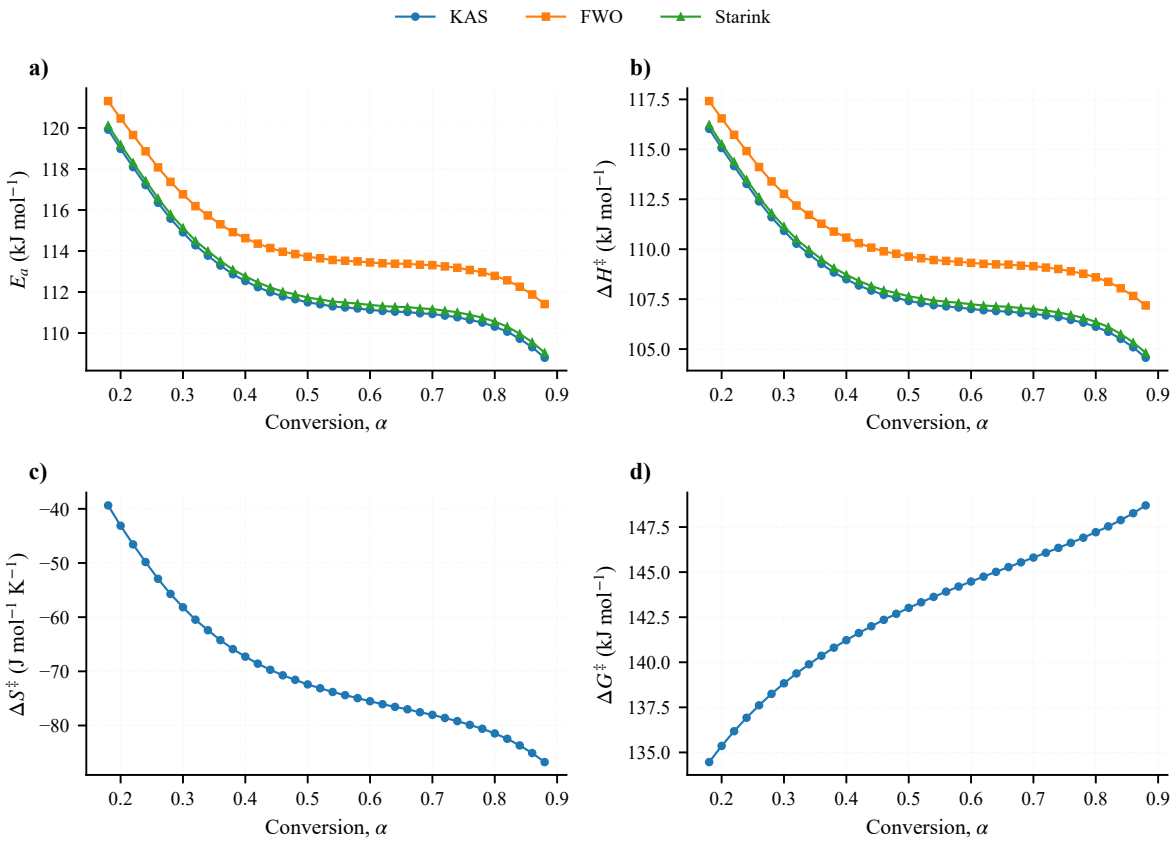

Fig. 13: *Isoconversional kinetic and thermodynamic analysis of SMP-10 with 0.3 nano particles. (a) Activation energy (E_a) as a function of the degree of conversion (α) obtained using the KAS, FWO, and Starink methods. (b) Enthalpy of activation ($\Delta H^{\ddagger}$) calculated from the corresponding E_a values using the temperature T_α derived from the KAS method. (c) Entropy of activation ($\Delta S^{\ddagger}$) determined from the KAS method. (d) Gibbs free energy of activation ($\Delta G^{\ddagger}$) determined from the KAS method.*

Table 2: *Kinetic and thermodynamic parameters for the curing of SMP-10 systems determined by isoconversional analysis.*

System	Method	E_a [kJ mol^{-1}]	$\Delta H^{\ddagger}$ [kJ mol^{-1}]	$\Delta S^{\ddagger}$ [J mol^{-1} K^{-1}]	$\Delta G^{\ddagger}$ [kJ mol^{-1}]
SMP-10 Pure	KAS	116 ± 5.9	111.9 ± 5.9	−63 ± 13	142.78 ± 0.32
	FWO	118 ± 5.7	113.9 ± 5.7	–	–
	Starink	122 ± 8.5	117.7 ± 8.5	–	–
0.1 SiC micro	KAS	92.5 ± 0.7	88.7 ± 0.7	-102 ± 5	136.14 ± 3.25
	FWO	95.3 ± 0.7	91.4 ± 0.7	–	–
	Starink	92.8 ± 0.7	88.9 ± 0.7	–	–
0.2 SiC micro	KAS	88.5 ± 2.2	84.6 ± 2.2	-111 ± 4	136.25 ± 3.51
	FWO	91.4 ± 2.3	87.6 ± 2.2	–	–
	Starink	88.7 ± 2.2	84.8 ± 2.2	–	–
0.3 SiC micro	KAS	85.8 ± 1.7	82.0 ± 1.7	-117 ± 6	136.43 ± 3.69
	FWO	88.9 ± 1.7	85.1 ± 1.6	–	–
	Starink	86.1 ± 1.7	82.2 ± 1.7	–	–
0.1 SiC nano	KAS	120.8 ± 1.6	116.8 ± 1.5	-49 ± 2	140.33 ± 2.21
	FWO	122.5 ± 1.6	118.4 ± 1.5	–	–
	Starink	121.0 ± 1.6	117.0 ± 1.5	–	–
0.2 SiC nano	KAS	114.7 ± 14.5	110.7 ± 14.4	-64 ± 26	141.37 ± 2.60
	FWO	116.7 ± 14.0	112.7 ± 13.9	–	–
	Starink	115.0 ± 14.5	110.9 ± 14.4	–	–
0.3 SiC nano	KAS	112.4 ± 2.8	108.3 ± 2.9	-70 ± 12	142.89 ± 4.00
	FWO	114.5 ± 2.5	110.5 ± 2.6	–	–
	Starink	112.6 ± 2.8	108.5 ± 2.9	–	–

The apparent activation energies obtained from the isoconversional analysis show a clear dependence on both filler size and filler loading, as summarized in Table 2. For the micro-SiC-filled systems, the average activation energy is consistently lower than that of pure SMP-10 and decreases progressively with increasing particle content. Specifically, the KAS-derived activation energy decreases from 116 ± 5.9 kJ mol^{-1} for pure SMP-10 to 92.5 ± 0.7 kJ mol^{-1}, 88.5 ± 2.2 kJ mol^{-1}, and 85.8 ± 1.7 kJ mol^{-1} for 0.1, 0.2, and 0.3 micro-SiC contents, respectively. Comparable trends are obtained from the FWO and Starink methods, confirming the consistency of the observed reduction in activation energy.

The reduction in activation energy for the micro-filled systems indicates that micro-sized SiC particles facilitate the curing process under non-isothermal conditions through physical effects rather than chemical modification of the curing mechanism. The presence of rigid micro-particles enhances heat transfer and reduces the effective fraction of reactive polymer, thereby lowering the apparent energetic barrier required for network formation.

In contrast, the nano-SiC-filled systems exhibit higher activation energies relative to both the pure polymer and the micro-filled systems. The KAS-derived activation energy increases to 120.8 ± 1.6 kJ mol^{-1} for 0.1 nano-SiC and remains elevated at 114.7 ± 14.5 kJ mol^{-1} and 112.4 ± 2.8 kJ mol^{-1} for 0.2 and 0.3 nano-SiC, respectively. These values are consistently higher than those of the corresponding micro-filled at comparable filler loadings.

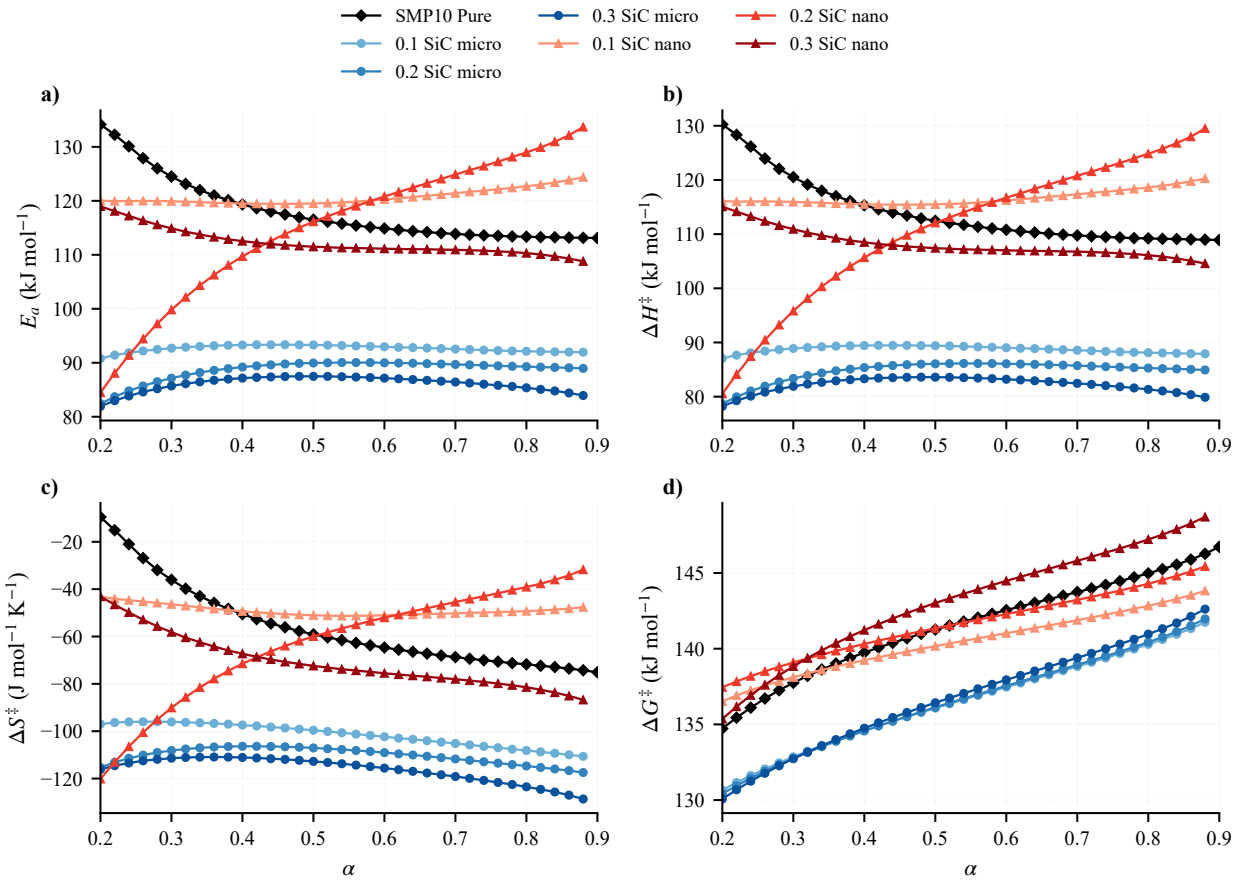

Fig. 14: *Isoconversional kinetic and thermodynamic data comparison. (a) Activation energy (E_a) as a function of the degree of conversion (α) obtained using the KAS, FWO, and Starink methods. (b) Enthalpy of activation ($\Delta H^{\ddagger}$) calculated from the corresponding E_a values using the temperature T_α derived from the KAS method. (c) Entropy of activation ($\Delta S^{\ddagger}$) determined from the KAS method. (d) Gibbs free energy of activation ($\Delta G^{\ddagger}$) determined from the KAS method.*

The conversion-dependent evolution of the activation energy further highlights the distinct role of particle size, as shown in Figure 14a. The micro-SiC-filled systems exhibit relatively low activation energies with only a weak dependence on conversion over the main curing range ($\alpha \approx 0.2$–0.9), indicating a kinetically stable curing process controlled by a single dominant reaction mechanism. In contrast, the nano-SiC-filled systems display higher activation energies across the entire conversion range, particularly at higher degrees of conversion, reflecting increasing kinetic resistance as curing progresses. The elevated activation energies observed for the nano-filled systems are attributed to strong polymer–particle interfacial interactions arising from the high specific surface area of nano-sized SiC particles. These interactions restrict polymer chain mobility near the filler surface, increasing the thermal energy required to achieve effective crosslinking and leading to the higher apparent activation energies observed in both Table 2 and Figure 14a.

Enthalpy of activation ($\Delta H^{\ddagger}$)

The enthalpy of activation follows trends analogous to those observed for the activation energy, as expected from the relation $\Delta H^{\ddagger} = E_a - RT$. For the micro-SiC-filled systems, $\Delta H^{\ddagger}$ decreases relative to pure SMP-10 and continues to decrease with increasing particle loading. Specifically, the KAS-derived enthalpy of activation decreases from 111.9 ± 5.9 kJ mol^{-1} for pure SMP-10 to 88.7 ± 0.7 kJ mol^{-1}, 84.6 ± 2.2 kJ mol^{-1}, and 82.0 ± 1.7 kJ mol^{-1} for 0.1, 0.2, and 0.3 micro-SiC contents, respectively as shown in (Table 2). This reduction confirms a lowered energetic

barrier for curing in the presence of micro-sized fillers and indicates that the energetic barrier associated with bond rearrangement during crosslinking is reduced. This suggests that micro-SiC particles facilitate the formation of the activated complex, likely through heterogeneous interfacial effects that promote local polymer rearrangements.

In contrast, the nano-SiC-filled systems exhibit consistently higher enthalpies of activation than both the pure polymer and the corresponding micro-filled systems. The KAS-derived $\Delta H^{\ddagger}$ increases to 116.7 ± 1.6 kJ mol^{-1} for the 0.1 nano-SiC system and remains elevated at 110.5 ± 14.5 kJ mol^{-1} and 108.3 ± 2.8 kJ mol^{-1} for the 0.2 and 0.3 nano-SiC compositions, respectively. As illustrated in Figure 14b, these higher $\Delta H^{\ddagger}(\alpha)$ values persist across the entire conversion range, reflecting increased energetic requirements for curing due to restricted molecular rearrangements associated with strong polymer–particle interfacial interactions.

Entropy of activation ($\Delta S^{\ddagger}$)

Negative values of the activation entropy ($\Delta S^{\ddagger}$) are observed for all systems, indicating that the transition state is more ordered than the reactant state, which is typical for crosslinking reactions involving network formation. For the micro-SiC-filled systems, the magnitude of $\Delta S^{\ddagger}$ becomes progressively more negative with increasing particle content, changing from -63 ± 13 J mol^{-1} K^{-1} for pure SMP-10 to -117 ± 6 J mol^{-1} K^{-1} for the 0.3 micro-SiC composition (Table 2). This trend indicates a more ordered transition state, consistent with the limited mobility of polymer chains caused by rigid micro-sized fillers during network formation.

In contrast, the nano-SiC-filled systems show less negative $\Delta S^{\ddagger}$ values at low filler loadings. Strong polymer–particle interfacial interactions limit the conformational freedom of polymer chains before the transition state is reached. As the nano-SiC content increases, $\Delta S^{\ddagger}$ becomes more negative, which is consistent with reduced polymer chain mobility as curing proceeds. These trends are consistent with the conversion-dependent entropy profiles shown in Figure 14c.

Gibbs free energy of activation ($\Delta G^{\ddagger}$)

Despite the variations observed in the activation energy, enthalpy, and entropy of activation, the Gibbs free energy of activation ($\Delta G^{\ddagger}$) remains relatively constant across all investigated systems, with values ranging from approximately 136 to 143 kJ mol^{-1} (Table 2). The small change in the values indicates enthalpy–entropy compensation as well as the increasing energetic difficulty of network formation as polymer mobility decreases during curing.

As shown in Figure 14d, $\Delta G^{\ddagger}(\alpha)$ exhibits only minor dependence on conversion and particle size, indicating that the overall thermodynamic feasibility of the curing reaction is not fundamentally altered by the addition of SiC fillers. Instead, particle size and loading primarily influence the reaction kinetics and pathway through changes in enthalpic and entropic contributions rather than through changes in the overall driving force for curing. Despite the differences in activation energies and thermodynamic parameters, the general curing mechanism remains consistent with the crosslinking reactions of AHPCS systems, indicating that filler particles primarily influence the energetics of network formation rather than altering the fundamental reaction pathway.

4.3 Determination of the Curing Mechanism

The curing mechanism of SMP-10-based systems filled with micro- and nano-sized SiC particles was investigated using the master plot method. Experimental master plots were constructed from non-isothermal DSC data and normalized at a reference conversion ($\alpha = 0.5$). These plots were compared with a set of theoretical kinetic models representing different solid-state reaction mechanisms. The agreement between experimental and theoretical curves was quantified using the root mean square error (RMSE), and the model with the lowest RMSE was identified as the dominant curing mechanism.

The master plot method is a model-fitting approach recommended by the ICTAC Kinetics Committee for identifying the most probable reaction mechanism once the activation energy as a function of conversion has been determined by an isoconversional method[53]. In this approach, experimental reduced-rate functions are normalized at a reference conversion and compared with theoretical master curves corresponding to ideal solid-state kinetic models. The validity of the method depends on the reliability of the isoconversional activation energy and on the assumption

that the pre-exponential factor does not vary significantly with conversion.

Recent analyses have shown that the applicability of the master plot method must be evaluated carefully, particularly when significant compensation effects or strong conversion dependence of kinetic parameters are present. Luo et al. demonstrated through simulated datasets that variations in the frequency factor can distort the reconstructed master plots, potentially leading to misidentification of the kinetic mechanism. Therefore, mechanistic interpretation requires simultaneous consideration of conversion-dependent activation energy trends and statistical agreement metrics [46].

Micro-sized SiC filled systems. For all micro-SiC filled formulations, the experimental master plots show the best agreement with Avrami–Erofeev type models, indicating that the curing reaction proceeds primarily through nucleation and growth processes throughout the investigated conversion range. In the context of polymer crosslinking, this behavior reflects the formation of localized crosslinking clusters that subsequently propagate through the polymer matrix as the reaction progresses. This mechanistic interpretation is also consistent with the activation-energy behavior obtained from the isoconversional analysis in Section 4.2. The relatively weak dependence of the apparent activation energy on conversion for the micro-SiC-filled systems indicates that the curing reaction proceeds through a single dominant kinetic regime. Such behavior is characteristic of nucleation-and-growth-type processes, where crosslinking centers form and expand throughout the polymer matrix without a significant transition to diffusion-controlled kinetics.

In the present study, the master plot analysis was performed using activation energies obtained from isoconversional methods and experimental DSC conversion data under multiple heating rates. The experimental master plots were quantitatively compared to theoretical Avrami–Erofeev (A2, A3), reaction-order (F_n), and diffusion-controlled (D_n) models. The model yielding the lowest RMSE over the investigated conversion range was identified as the dominant kinetic pathway. High-conversion regions were examined for systematic deviations, since such deviations can indicate diffusion limitations, vitrification, or reduced polymer chain mobility caused by filler particles. For the 0.1 micro-SiC formulation (Figure 15a), the experimental master plot closely follows the Avrami–Erofeev A2 model across the entire conversion range, with minimal deviation at both low and high α. The relatively low RMSE (0.212) indicates that curing proceeds via progressive nucleation followed by two-dimensional growth of crosslinked domains. No significant deviation appears at high conversion, which indicates weak diffusion limitations and preserved polymer chain mobility at low filler loading.

At intermediate micro-SiC loading (0.2, Figure 15c), the A3 model shows improved agreement (RMSE = 0.279), indicating increased dimensionality of growth processes during network formation. The shift from A2 to A3 behavior suggests that filler particles may facilitate additional heterogeneous nucleation sites, promoting more spatially extended crosslink propagation. However, the overall nucleation-and-growth mechanism remains dominant. For the highest micro-SiC content (0.3, Figure 15e), both models A2 and A3 shows comparable RMSE fits ≈ 0.30, confirming that increasing micro-particle loading does not fundamentally alter the curing mechanism. The persistence of Avrami-type behavior across all micro-filled systems indicates that microscale particles primarily act as inert physical inclusions rather than strongly restricting chain mobility. This is because micro-sized SiC particles provide relatively small interfacial surface area compared with nano-particles, and their influence on polymer chain mobility and crosslinking pathways remains limited. As a result, the curing reaction retains the same nucleation-and-growth behavior observed in the unfilled SMP-10 system.

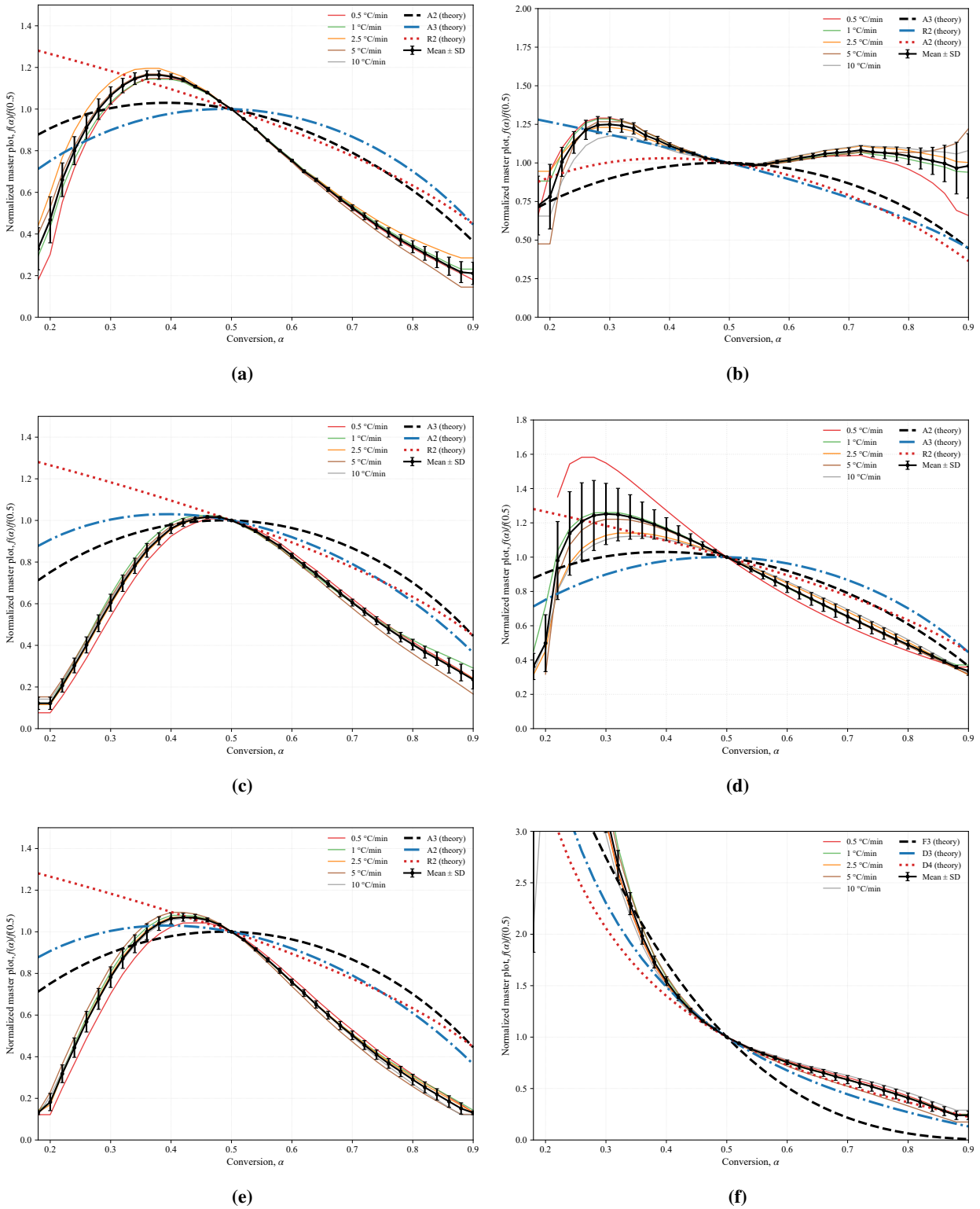

Fig. 15: *Master plot comparison between experimental data and theoretical kinetic models for SMP-10 systems filled with SiC particles: (a) 0.1 micro-SiC, (b) 0.1 nano-SiC, (c) 0.2 micro-SiC, (d) 0.2 nano-SiC, (e) 0.3 micro-SiC, and (f) 0.3 nano-SiC.*

Nano-sized SiC filled systems. Nano-SiC filled systems show a clear dependence of the curing mechanism on filler content. The high specific surface area of nano-sized particles increases polymer–particle interfacial interactions and reduces polymer chain mobility.

At low nano-SiC loading (0.1, Figure 15b), the A3 model gives the lowest RMSE (0.253), which corresponds to nucleation-and-growth-controlled curing similar to the micro-filled systems. Small deviations at intermediate conversion occur and are associated with polymer–particle interfacial interactions arising from the large surface area of nanoscale fillers. For the 0.2 nano-SiC formulation (Figure 15d), the A2 model gives the best fit (RMSE = 0.170), the lowest error among all investigated systems. The agreement of the curves in the low-conversion region corresponds to nucleation-dominated kinetics influenced by polymer–particle interfaces. The low RMSE also corresponds to more uniform nucleation while polymer chain mobility remains sufficient for growth.

At the highest nano-SiC loading (0.3, Figure 15f), the curing mechanism shifts toward reaction-order behavior, and the F3 model gives the lowest RMSE (0.677). The deviation from Avrami-type curves at higher conversion results from reduced polymer chain mobility and suppression of growth processes caused by formation of a dense nanoparticle network. This behavior is consistent with diffusion limitations and vitrification effects observed in highly filled polymer systems. The best-fitting model and the corresponding RMSE for each formulation are summarized in Table 3, while the full RMSE comparison across all candidate models is provided in Table 4. The complete comparison confirms that the Avrami–Erofeev models (A2/A3) yield the lowest RMSE for all micro-SiC systems and for the 0.1 and 0.2 nano-SiC systems, whereas the reaction-order model F3 provides the lowest RMSE only at the highest nano-SiC loading (0.3 nano-SiC).

Table 3: *Summary of master plot analysis results for SMP-10 systems filled with micro- and nano-sized SiC particles.*

Sample	Filler type	Best model	RMSE	Dominant mechanism
0.1 SiC micro	Micro	A2	0.212	Nucleation and growth
0.2 SiC micro	Micro	A3	0.279	Nucleation and growth
0.3 SiC micro	Micro	A3	0.297	Nucleation and growth
0.1 SiC nano	Nano	A3	0.253	Nucleation and growth
0.2 SiC nano	Nano	A2	0.170	Nucleation and growth
0.3 SiC nano	Nano	F3	0.677	Reaction-order controlled

Table 4: *Root mean square error (RMSE) between the experimental master plots and all candidate kinetic models for SMP-10 systems filled with micro- and nano-sized SiC particles. The lowest (best-fitting) RMSE in each column is shown in bold.*

	Micro-SiC			Nano-SiC		
Model	**0.1**	**0.2**	**0.3**	**0.1**	**0.2**[†]	**0.3**
F1	0.372	0.560	0.505	0.443	0.312	1.527
F2	0.750	0.953	0.884	0.798	0.694	1.172
F3	1.334	1.538	1.469	1.325	1.270	**0.677**
A2	**0.212**	0.310	0.300	0.274	**0.170**	1.797
A3	0.245	**0.279**	**0.297**	**0.253**	0.214	1.865
R2	0.298	0.440	0.415	0.273	0.221	1.667
R3	0.307	0.470	0.433	0.332	0.235	1.622
D1	0.693	0.864	0.824	0.596	0.612	1.254
D2	0.894	1.078	1.026	0.842	0.823	1.041
D3	1.192	1.381	1.323	1.153	1.126	0.780
D4	0.986	1.172	1.118	0.943	0.918	0.955
Best	**A2**	**A3**	**A3**	**A3**	**A2**	**F3**

[†] For the 0.2 nano-SiC sample, a single representative activation energy at $\alpha = 0.5$ was used in the master plot construction (see Methodology), owing to the strong conversion dependence of $E_a(\alpha)$ for this formulation. All other parameters were identical to those used for the remaining formulations.

These mechanistic assignments are based on the apparent kinetic behavior obtained from thermal analysis. The interpretation is consistent across the kinetic, thermodynamic, and master plot analyses, although direct molecular-level confirmation of bond evolution during curing was not within the scope of the present study.

To facilitate visualization of the proposed physical interpretation of the observed curing behavior, a conceptual schematic is presented in Figure 16. The illustration summarizes the proposed roles of micro- and nano-sized SiC particles during SMP-10 curing based on the DSC-derived kinetic, thermodynamic, and master plot analyses. The schematic is intended as a conceptual representation of the proposed physical effects and does not represent direct experimental evidence of the underlying molecular interactions.

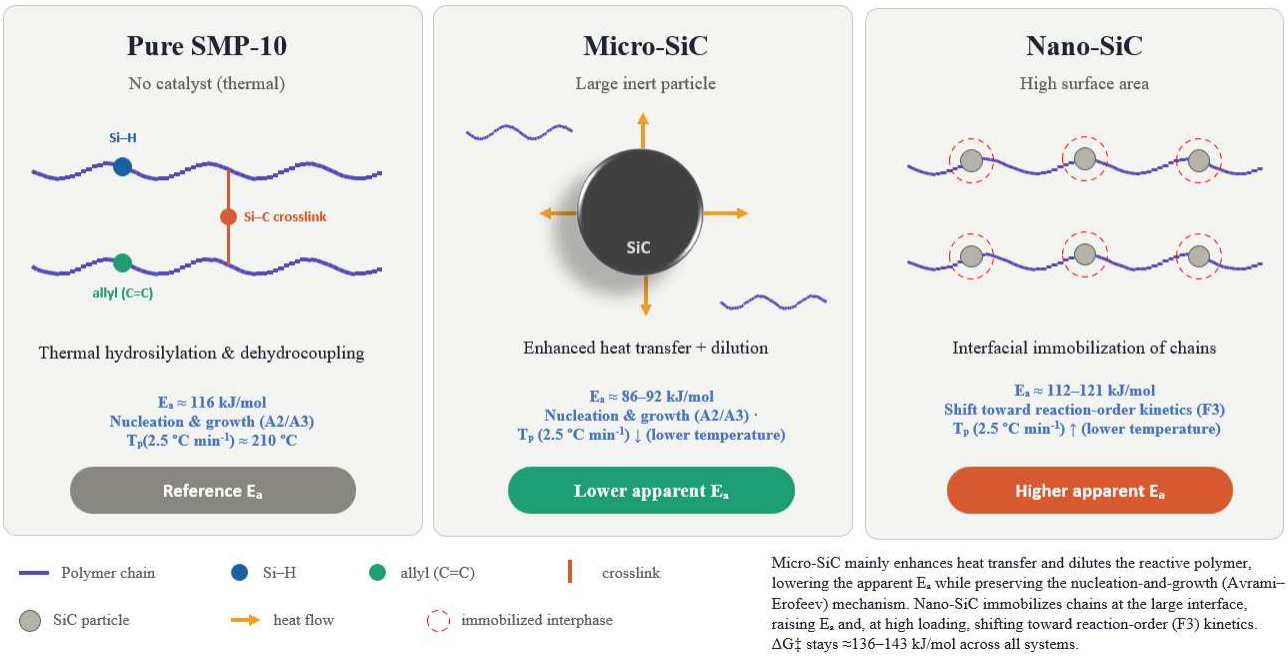

Fig. 16: *Schematic representation of the proposed effect of SiC particle size on the curing behavior of SMP-10.*

4.4 Implications for SiC matrix composite processing

The results show that micro-SiC fillers preserve nucleation and growth-controlled curing behavior across all investigated loadings, providing a stable and predictable curing mechanism. In contrast, nano-SiC fillers induce a transition in the curing mechanism at high loadings, which may narrow the processing window and require stricter thermal control. These findings support the design and processing of SMP-10-derived SiC matrix composites, where controlled curing is important for achieving defect-free microstructures prior to pyrolysis.

The combined DSC-based conversion analysis, isoconversional kinetics, transition-state thermodynamics, and master plot analysis show that the curing response of SMP-10 varies with SiC particle size and loading. Representative DSC thermograms and conversion profiles (**Figs.** 1–7) confirm that increasing heating rate systematically shifts the curing exotherm to higher temperatures particle size and loading. At comparable filler loadings, the nano-filled systems exhibit a larger temperature shift than the micro-filled systems.

Energetic barrier: micro-SiC lowers E_a, nano-SiC maintains higher E_a. Peak-based and isoconversional results show that micro-sized SiC reduces the apparent energetic barrier relative to pure SMP-10, whereas nano-sized SiC yields higher activation energies than micro-filled systems. In particular, the KAS-derived average E_a decreases

from 116 kJ mol^{-1} for pure SMP-10 to 92.5, 88.5, and 85.8 kJ mol^{-1} for 0.1, 0.2, and 0.3 micro-SiC formulations, respectively (**Table** 2). In contrast, nano-SiC formulations exhibit higher KAS-derived E_a values (120.8 kJ/mol for 0.1 nano, 114.7 kJ mol^{-1} for 0.2 nano, and 112.4 kJ mol^{-1} for 0.3 nano; **Table** 2), indicating that nanoscale fillers impose a substantially stronger kinetic constraint than microscale fillers. The large standard deviation observed for 0.2 nano-SiC ($\pm$14.5 kJ mol^{-1}) further highlights that the nano-filled systems are more sensitive to conversion-dependent effects and/or experimental dispersion in T_α (**Figs.** 12 and 14).

Thermodynamic compensation: similar $\Delta G^\ddagger$ despite different E_a. Although E_a, $\Delta H^\ddagger$, and $\Delta S^\ddagger$ vary substantially across formulations, the Gibbs free energy of activation remains within a relatively narrow interval ($\sim$ 136–143 kJ mol^{-1}; **Table** 2). These results indicate enthalpy–entropy compensation. Micro- and nano-sized fillers modify the kinetic pathway and polymer chain mobility during curing, while the overall thermodynamic feasibility of network formation remains similar among the systems. Practically, this means that fillers primarily tune *how* curing proceeds (rate and pathway) rather than whether curing can occur under the studied thermal schedules.

Mechanistic pathway: Avrami–Erofeev for micro systems; mechanism shift at high nano loading. Master plot analysis (**Figs.** 15a–15f and **Table** 3) shows that all micro-SiC formulations are best described by Avrami–Erofeev type kinetics (A2/A3; RMSE $\approx$ 0.21–0.30), supporting a nucleation-and-growth dominated curing mechanism across micro-filler loadings. Nano-SiC formulations exhibit a stronger loading dependence: 0.1 nano and 0.2 nano remain best described by A-type models (A3 and A2, respectively; RMSE 0.253 and 0.170), whereas the highest nano loading (0.3 nano) shifts toward reaction-order behavior with F3 providing the best fit (RMSE 0.677). This transition indicates that increasing nano content changes the dominant rate-controlling features of curing, consistent with progressively restricted segmental mobility and reduced freedom for spatial growth as the filler interfacial area and particle connectivity increase.

Relevance for SiC-matrix composite manufacturing from SMP-10 precursors. For polymer-derived ceramic processing routes, controlled curing is important for achieving a robust green body prior to pyrolysis. The present results establish a quantitative basis for selecting filler size and loading to tailor cure behavior: micro-SiC systematically lowers E_a and preserves Avrami-type kinetics, which is favorable for predictable cure progression and a broader processing window. This reduction in apparent activation energy therefore suggests that curing can proceed at slightly lower temperatures or shorter dwell times without altering the dominant reaction mechanism. From a processing perspective, this behavior is advantageous for PIP-based composite fabrication, as it promotes more uniform crosslinking within infiltrated fiber preforms and reduces the likelihood of thermal gradients that can generate microcracking during curing. In contrast, nano-SiC introduces a substantially higher kinetic barrier and, at high loading, alters the apparent mechanism toward reaction-order control, implying increased sensitivity of the cure rate to conversion and potentially tighter requirements on heating schedules. Although nano-SiC particles may contribute to improved packing density during later densification stages, the higher activation energies and delayed curing onset indicate that greater thermal input is required to achieve comparable conversion levels. In PIP processing, this may necessitate longer curing dwell times or higher temperatures to ensure complete crosslinking throughout the composite preform. Therefore, the combined kinetic–mechanistic framework established here enables rational formulation design of SMP-10/SiC systems to balance cure control, processability, and the requirements of subsequent SiC-matrix composite fabrication. From a practical standpoint, these kinetic differences translate into distinct processing considerations for the two filler types. The lower apparent activation energy of the micro-SiC systems implies that a comparable degree of cure can in principle be reached at slightly lower hold temperatures or with shorter dwell times, which would reduce the thermal budget of the curing step and the temperature gradients associated with residual thermal stress, particularly in thick or geometrically complex preforms. Because the micro-SiC systems retain Avrami–Erofeev kinetics across all investigated loadings, the cure progression remains predictable, which is advantageous during the early PIP cycles where uniform, low-stress crosslinking of the infiltrated polymer helps preserve green-body integrity prior to pyrolysis. In contrast, the higher activation energies and delayed curing exotherms of the nano-SiC systems indicate that higher hold temperatures or longer dwell times would be required to achieve complete crosslinking, particularly at the highest loading where the dominant mechanism shifts toward reaction-order behavior. The narrower curing exotherms of the nano-filled systems are also consistent with a more limited temperature interval over which curing occurs, which may place tighter requirements on thermal control. Overall, the present results suggest that micro-SiC is associated with a broader and

more predictable curing window suited to multi-cycle PIP processing, whereas nano-SiC requires greater thermal input and closer control of the curing schedule. A full assessment of infiltration behavior and densification efficiency would require dedicated processing trials, which are beyond the scope of the present kinetic study.

5 Conclusions

This study provides a systematic investigation of how SiC particle size (micro vs. nano) and loading influence the non-isothermal curing behavior of the allyl-functionalized preceramic polymer SMP-10. Through DSC-based conversion analysis, model-free isoconversional kinetics (KAS, FWO, Starink), transition-state thermodynamic evaluation, and master plot model analysis, this work establishes a mechanistic framework for understanding how filler size influences curing kinetics and network formation in particle-modified preceramic polymers

1. Particle-Size-Dependent Kinetic Behavior: The curing response of SMP-10 is strongly influenced by the size of incorporated SiC particles. Micro-sized SiC reduces the apparent activation energy relative to pure SMP-10, whereas nano-sized SiC maintains higher activation energies and introduces stronger conversion dependence. These differences are attributed to physical effects of the filler (enhanced heat transfer and dilution for micro-SiC, and restricted interfacial mobility for nano-SiC) rather than to a change in the intrinsic curing chemistry, consistent with the unchanged nucleation-and-growth mechanism identified for the filled systems.
2. Enthalpy–Entropy Compensation in Filled Systems: Despite substantial variations in activation energy (E_a), enthalpy ($\Delta H^{\ddagger}$), and entropy of activation ($\Delta S^{\ddagger}$) across the investigated formulations, the Gibbs free energy of activation ($\Delta G^{\ddagger}$) remains within a relatively narrow range. This behavior reflects a classical enthalpy–entropy compensation effect, indicating that changes in filler size alter the energetic pathway of network formation while the overall thermodynamic barrier governing the curing reaction remains comparable.
3. Mechanistic Differences between Micro- and Nano-Filled Systems: Master plot analysis shows that micro-SiC-filled systems follow nucleation-and-growth dominated kinetics described by Avrami–Erofeev models across the investigated loading range. This behavior is consistent with the relatively weak conversion dependence of the apparent activation energy observed in the isoconversional analysis. In contrast, nano-SiC systems exhibit a stronger dependence on filler loading, with the highest nano content showing behavior consistent with reaction-order kinetics. This shift suggests that increasing nano-particle content progressively restricts segmental mobility and limits spatial growth processes during curing.
4. Implications for Preceramic Polymer Processing: These findings highlight the importance of particle size in controlling curing behavior in particle-enhanced SMP-10 systems. Micro-SiC promotes a relatively stable curing pathway with reduced kinetic barriers, whereas nano-SiC introduces stronger interfacial constraints that may require tighter thermal control during processing. Understanding these effects provides a framework for selecting filler size and loading to tailor curing schedules and processing conditions in polymer infiltration and pyrolysis (PIP) routes for SiC-matrix composites.

Acknowledgments

This material is based upon work supported by the Air Force Office of Scientific Research under award number FA9550-24-1-0212.

References

[1] C. Zweben. Advanced composites for aerospace applications. *Composites*, 12(4):235–240, October 1981. Publisher: Elsevier BV. URL: https://linkinghub.elsevier.com/retrieve/pii/0010436181900112, doi:10.1016/0010-4361(81)90011-2.

[2] Kunjie Wang, Chenghai Xu, Bo Gao, Leying Song, and Songhe Meng. Analysis of the fracture behavior and mechanism of PIP-C/SiC composites at high temperatures. *Composite Structures*, 348:118491, November 2024. Publisher: Elsevier BV. URL: https://linkinghub.elsevier.com/retrieve/pii/S0263822324006196, doi:10.1016/j.compstruct.2024.118491.

[3] G. Ziegler, I. Richter, and D. Suttor. Fiber-reinforced composites with polymer-derived matrix: processing, matrix formation and properties. *Composites Part A: Applied Science and Manufacturing*, 30(4):411–417, April

1999. URL: https://linkinghub.elsevier.com/retrieve/pii/S1359835X98001286, doi:10.1016/S1359-835X(98)00128-6.

[4] Derek King, Zlatomir Apostolov, Thomas Key, Carmen Carney, and Michael Cinibulk. Novel processing approach to polymer-derived ceramic matrix composites. *International Journal of Applied Ceramic Technology*, 15(2):399–408, March 2018. URL: https://ceramics.onlinelibrary.wiley.com/doi/10.1111/ijac.12805, doi:10.1111/ijac.12805.

[5] R. Sreeja, B. Swaminathan, Anil Painuly, T.V. Sebastian, and S. Packirisamy. Allylhydridopolycarbosilane (AHPCS) as matrix resin for C/SiC ceramic matrix composites. *Materials Science and Engineering: B*, 168(1-3):204–207, April 2010. URL: https://linkinghub.elsevier.com/retrieve/pii/S0921510709005583, doi:10.1016/j.mseb.2009.12.033.

[6] Stefano Mungiguerra, Giuseppe D. Di Martino, Raffaele Savino, Luca Zoli, Laura Silvestroni, and Diletta Sciti. Characterization of novel ceramic composites for rocket nozzles in high-temperature harsh environments. *International Journal of Heat and Mass Transfer*, 163:120492, 2020. URL: https://www.sciencedirect.com/science/article/pii/S0017931020334281, doi:10.1016/j.ijheatmasstransfer.2020.120492.

[7] Sheng Zhang, Yuchun Feng, Xiguang Gao, Yingdong Song, Fang Wang, and Shirong Zhang. Modeling of fatigue failure for sic/sic ceramic matrix composites at elevated temperatures and multi-scale experimental validation. *Journal of the European Ceramic Society*, 42(8):3395–3403, 2022. URL: https://www.sciencedirect.com/science/article/pii/S0955221922001546, doi:10.1016/j.jeurceramsoc.2022.02.049.

[8] Mosiur Rahaman, Mark Olima, Jacob McCormick, Sanwu Wang, Matthew R. Ryder, Michael W. Keller, and Hema Ramsurn. A systematic approach to enhancing the oxidation resistance of c/c composites using multi-layer sic–zrb_2-based coatings. *Journal of the European Ceramic Society*, page 118372, 2026. URL: https://www.sciencedirect.com/science/article/pii/S0955221926002487, doi:10.1016/j.jeurceramsoc.2026.118372.

[9] Fabia Süß, Tobias Schneider, Martin Frieß, Raouf Jemmali, Felix Vogel, Linda Klopsch, and Dietmar Koch. Combination of PIP and LSI processes for SiC/SiC ceramic matrix composites. *Open Ceramics*, 5:100056, March 2021. URL: https://linkinghub.elsevier.com/retrieve/pii/S266653952100002X, doi:10.1016/j.oceram.2021.100056.

[10] Slavica Porobic Katnic, Mohammed Ammar Abdul Latheef, Keri Sharp, Ramona Naghi, Mark Olima, Hema Ramsurn, William LePage, and Michael W. Keller. Addressing processing limitations in SiC-based ceramic composites: A review of hybrid approaches and perspectives. *Ceramics International*, 51(30):63501–63518, 2025. URL: https://www.sciencedirect.com/science/article/pii/S0272884225049181, doi:10.1016/j.ceramint.2025.10.067.

[11] Dachamir Hotza, Rafael K. Nishihora, Ricardo A. F. Machado, Pierre-Marie Geffroy, Thierry Chartier, and Samuel Bernard. Tape casting of preceramic polymers toward advanced ceramics: A review. *International Journal of Ceramic Engineering & Science*, 1(1):21–41, May 2019. URL: https://ceramics.onlinelibrary.wiley.com/doi/10.1002/ces2.10009, doi:10.1002/ces2.10009.

[12] Lewis J. Print, John J. Liggat, Stan Moug, Helen Seaton, and David C. Apperley. A Study of the Ceramicisation of Allylhydridopolycarbosilane by Thermal Volatilisation Analysis and Solid-State Nuclear Magnetic Resonance. *Silicon*, 15(3):1355–1379, February 2023. URL: https://link.springer.com/10.1007/s12633-022-02072-0, doi:10.1007/s12633-022-02072-0.

[13] I.C. McNeill. Thermal volatilization analysis of high polymers. *European Polymer Journal*, 3(3):409–421, 1967. URL: https://www.sciencedirect.com/science/article/pii/0014305767900110, doi:10.1016/0014-3057(67)90011-0.

[14] Zlatomir D. Apostolov, Elizabeth P. Heckman, Thomas S. Key, and Michael K. Cinibulk. Effects of low-temperature treatment on the properties of commercial preceramic polymers. *Journal of the European Ceramic Society*, 40(8):2887–2895, July 2020. URL: https://linkinghub.elsevier.com/retrieve/pii/S0955221920301230, doi:10.1016/j.jeurceramsoc.2020.02.030.

[15] Sarabjeet Kaur, Ralf Riedel, and Emanuel Ionescu. Pressureless fabrication of dense monolithic sic ceramics from a polycarbosilane. *Journal of the European Ceramic Society*, 34(15):3571–3578, 2014. URL: https://www.sciencedirect.com/science/article/pii/S0955221914002520, doi:10.1016/j.jeurceramsoc.2014.05.002.

[16] K. Kawamura, M. Ono, and K. Okazaki. Silicon carbide/carbon composite sheets derived from pcs/coal-tar pitch mixtures. *Carbon*, 30(3):429–434, 1992. URL: https://www.sciencedirect.com/science/article/pii/

000862239290041T, doi:10.1016/0008-6223(92)90041-T.

[17] Zhaoju Yu, Hao Min, Junying Zhan, and Le Yang. Preparation and dielectric properties of polymer-derived sicti ceramics. *Ceramics International*, 39(4):3999–4007, 2013. URL: https://www.sciencedirect.com/science/article/pii/S0272884212012138, doi:10.1016/j.ceramint.2012.10.250.

[18] L.V. Interrante, J.M. Jacobs, W. Sherwood, and C.W. Whitmarsh. Fabrication and Properties of Fiber- and Particulate-Reinforced SiC Matrix Composites Obtained with (A)HPCS as the Matrix Source. *Key Engineering Materials*, 127-131:271–278, November 1996. URL: https://www.scientific.net/KEM.127-131.271, doi:10.4028/www.scientific.net/KEM.127-131.271.

[19] Binjie Qian, Biwen Cao, Mingyu Chu, Yubing Li, Hanyu Ma, Rongye Guo, and Liqiang Wan. Curing reactions of liquid hydridopolycarbosilanes with vinyl or allyl groups. *Journal of Applied Polymer Science*, 140(42):e54565, November 2023. URL: https://onlinelibrary.wiley.com/doi/10.1002/app.54565, doi:10.1002/app.54565.

[20] Zhaoju Yu, Le Yang, Junying Zhan, Cong Zhou, Hao Min, Qiang Zheng, and Haiping Xia. Preparation, cross-linking and ceramization of AHPCS/Cp2ZrCl2 hybrid precursors for SiC/ZrC/C composites. *Journal of the European Ceramic Society*, 32(6):1291–1298, June 2012. URL: https://linkinghub.elsevier.com/retrieve/pii/S0955221911006649, doi:10.1016/j.jeurceramsoc.2011.12.015.

[21] Jingyao Hu, Chidong Liu, Fang Ye, Laifei Cheng, and Yucong Wei. A review on high-performance sicf/sic composites prepared by pip process. *Journal of Materials Research and Technology*, 33:7216–7235, 2024. URL: https://www.sciencedirect.com/science/article/pii/S223878542402578X, doi:10.1016/j.jmrt.2024.11.050.

[22] Suraj C. Zunjarrao, Arif Rahman, and Raman P. Singh. Characterization of the Evolution and Properties of Silicon Carbide Derived From a Preceramic Polymer Precursor. *Journal of the American Ceramic Society*, 96(6):1869–1876, June 2013. URL: https://ceramics.onlinelibrary.wiley.com/doi/10.1111/jace.12273, doi:10.1111/jace.12273.

[23] Slavica Porobic Katnic, Mohammed Ammar Abdul Latheef, Michael K. Cinibulk, William LePage, Michael W. Keller, and Hema Ramsurn. Curing mechanisms of an allyl-functionalized preceramic polymer with radical initiators: Kinetics and thermodynamics. *Journal of the American Ceramic Society*, 109(2):e70559, 2026. URL: https://ceramics.onlinelibrary.wiley.com/doi/abs/10.1111/jace.70559, arXiv:https://ceramics.onlinelibrary.wiley.com/doi/pdf/10.1111/jace.70559, doi:10.1111/jace.70559.

[24] Derek King, Zlatomir Apostolov, Thomas Key, Carmen Carney, and Michael Cinibulk. Novel processing approach to polymer-derived ceramic matrix composites. *International Journal of Applied Ceramic Technology*, 15(2):399–408, 2018. URL: https://ceramics.onlinelibrary.wiley.com/doi/abs/10.1111/ijac.12805, arXiv:https://ceramics.onlinelibrary.wiley.com/doi/pdf/10.1111/ijac.12805, doi:10.1111/ijac.12805.

[25] Can Akaoglu, Junquan Lao, Kerui Wei, Philip J. Withers, and Ping Xiao. Highly crystalline sicf/sic composites produced by particle enhanced polymer impregnation and pyrolysis (pe-pip). *Materials and Design*, 249:113551, 2025. URL: https://www.sciencedirect.com/science/article/pii/S0264127524009262, doi:10.1016/j.matdes.2024.113551.

[26] Kevin Moraes, Walter Sherwood, J.M. Jacobs, and Leonard Interrante. Effect of particulate fillers on the processing and properties of a fiber-reinforced polymer precursor derived sic-matrix composite. *Ceramic Engineering and Science Proceedings*, 21:289–295, 01 2000.

[27] Bartłomiej Kryszak, Aleksandra Ujčić, Veronika Gajdošová, Miroslav Šlouf, and Konrad Szustakiewicz. Micro vs nano: influence of filler size on the rheological and mechanical properties of highly-filled pla/hap and pcl/hap composites. *Journal of Materials Research and Technology*, 37:2919–2934, 2025. URL: https://www.sciencedirect.com/science/article/pii/S2238785425016576, doi:10.1016/j.jmrt.2025.06.234.

[28] Y Katoh, S.M Dong, and A Kohyama. Thermo-mechanical properties and microstructure of silicon carbide composites fabricated by nano-infiltrated transient eutectoid process. *Fusion Engineering and Design*, 61-62:723–731, 2002. URL: https://www.sciencedirect.com/science/article/pii/S0920379602001801, doi:10.1016/S0920-3796(02)00180-1.

[29] Junquan Lao, Can Akaoglu, Kerui Wei, Han Liu, Philip J. Withers, and Ping Xiao. The characterisation of sicf/sic composites made by conventional and particle enhanced polymer infiltration pyrolysis. *Journal of the European Ceramic Society*, 46(2):117789, 2026. URL: https://www.sciencedirect.com/science/article/pii/S0955221925006107, doi:10.1016/j.jeurceramsoc.2025.117789.

[30] Arulmozhivarman Joseph Chandran, Sanjay Mavinkere Rangappa, Indran Suyambulingam, and Suchart Siengchin. Micro/nano fillers for value-added polymer composites: A comprehensive review. *Journal of Vinyl and Additive Technology*, 30(5):1083–1123, 2024. URL: https://4spepublications.onlinelibrary.wiley.com/doi/abs/10.1002/vnl.22106, arXiv:https://4spepublications.onlinelibrary.wiley.com/doi/pdf/10.1002/vnl.22106, doi:10.1002/vnl.22106.

[31] Ke Jian, Zhao-Hui Chen, Qing-Song Ma, Hai-Feng Hu, and Wen-Wei Zheng. Processing and properties of 2d-cf/sic composites incorporating sic fillers. *Materials Science and Engineering: A*, 408(1):330–335, 2005. URL: https://www.sciencedirect.com/science/article/pii/S092150930501052X, doi:10.1016/j.msea.2005.08.205.

[32] Yang Zhao and Dietmar Drummer. Influence of filler content and filler size on the curing kinetics of an epoxy resin. *Polymers*, 11(11), 2019. URL: https://www.mdpi.com/2073-4360/11/11/1797, doi:10.3390/polym11111797.

[33] Andrzej Mianowski, Marek Sciazko, and Tomasz Radko. Vyazovkin's isoconversional method as a universal approach. *Thermochimica Acta*, 696:178822, 2021. URL: https://www.sciencedirect.com/science/article/pii/S0040603120307371, doi:10.1016/j.tca.2020.178822.

[34] Jose C. Cordeiro, Rachel E. Davis, Hema Ramsurn, Daniel W. Crunkleton, Todd P. Otanicar, and Michael W. Keller. Prediction of curing kinetics of resorcinol-added resole phenolic resins using differential scanning calorimetry for the fabrication of carbon/carbon composites. *Journal of Applied Polymer Science*, 139(39):e52949, 2022. URL: https://onlinelibrary.wiley.com/doi/abs/10.1002/app.52949, arXiv:https://onlinelibrary.wiley.com/doi/pdf/10.1002/app.52949, doi:10.1002/app.52949.

[35] H. E. Kissinger. Reaction Kinetics in Differential Thermal Analysis. *Analytical Chemistry*, 29(11):1702–1706, November 1957. Publisher: American Chemical Society (ACS). URL: https://pubs.acs.org/doi/abs/10.1021/ac60131a045, doi:10.1021/ac60131a045.

[36] Takeo Ozawa. A New Method of Analyzing Thermogravimetric Data. *Bulletin of the Chemical Society of Japan*, 38(11):1881–1886, November 1965. Publisher: Oxford University Press (OUP). URL: https://academic.oup.com/bcsj/article/38/11/1881/7369983, doi:10.1246/bcsj.38.1881.

[37] Elena Moukhina. Determination of kinetic mechanisms for reactions measured with thermoanalytical instruments. *Journal of Thermal Analysis and Calorimetry*, 109(3):1203–1214, September 2012. Publisher: Springer Science and Business Media LLC. URL: http://link.springer.com/10.1007/s10973-012-2406-3, doi:10.1007/s10973-012-2406-3.

[38] Đurica Katnić, Milena Marinović-Cincović, Slavica J. Porobić, Ivica Vujčić, Aleksandra Šaponjić, Biljana Sikirić, and Dragana Živojinović. Characterization and kinetics of thermal decomposition behavior of plum and fig pomace biomass. *Journal of Cleaner Production*, 352:131637, 2022. URL: https://www.sciencedirect.com/science/article/pii/S0959652622012537, doi:10.1016/j.jclepro.2022.131637.

[39] Bojana Milićević, Sanja Kuzman, Slavica J. Porobić, Milena Marinović-Cincović, and Miroslav D. Dramićanin. Non-isothermal crystallization kinetics of the heavy-group lanthanide dititanates. *Optical Materials*, 74:86–92, 2017. Special Issue of 6th International Conference of Excited States of Transition Elements and Workshop on Luminescence (ESTE 2016). URL: https://www.sciencedirect.com/science/article/pii/S0925346717302070, doi:10.1016/j.optmat.2017.03.058.

[40] T. Akahira and T. Sunose. Joint convention of four electrical institutes. Research report, Chiba Institute of Technology, Chiba, 1971.

[41] J. H. Flynn and L. A. Wall. A quick, direct method for the determination of activation energy from thermogravimetric data. *Polymer Letters*, 4:323–328, 1966.

[42] M.J Starink. The determination of activation energy from linear heating rate experiments: a comparison of the accuracy of isoconversion methods. *Thermochimica Acta*, 404(1-2):163–176, September 2003. Publisher: Elsevier BV. URL: https://linkinghub.elsevier.com/retrieve/pii/S0040603103001448, doi:10.1016/s0040-6031(03)00144-8.

[43] Cheng Tung Chong, Guo Ren Mong, Jo-Han Ng, William Woei Fong Chong, Farid Nasir Ani, Su Shiung Lam, and Hwai Chyuan Ong. Pyrolysis characteristics and kinetic studies of horse manure using thermogravimetric analysis. *Energy Conversion and Management*, 180:1260–1267, 2019. URL: https://www.sciencedirect.com/science/article/pii/S0196890418313232, doi:10.1016/j.enconman.2018.11.071.

[44] Ajay Sharma and Bikash Mohanty. Non-isothermal tg/dtg-ftir kinetic study for devolatilization of dalbergia sissoo wood under nitrogen atmosphere. *Journal of Thermal Analysis and Calorimetry*, 146(2):865–879, 2021. doi:10.1007/s10973-020-09978-0.

[45] Ammar Khawam and Douglas R. Flanagan. Solid-state kinetic models:basics and mathematical fundamentals. *The Journal of Physical Chemistry B*, 110(35):17315–17328, 2006. doi:10.1021/jp062746a.

[46] Laipeng Luo, Zhiyi Zhang, Chong Li, Nishu, Fang He, Xingguang Zhang, and Junmeng Cai. Insight into master plots method for kinetic analysis of lignocellulosic biomass pyrolysis. *Energy*, 233:121194, 2021. URL: https://www.sciencedirect.com/science/article/pii/S0360544221014420, doi:10.1016/j.energy.2021.121194.

[47] Changwei Liu, Chunyan Qu, Chengyang Wang, Dianxue Cao, Dezhi Wang, Wanbao Xiao, Hao Feng, Ping Liu, and Xuefeng Bai. Non-isothermal curing kinetics, chemorheological behaviour, and ir spectral study of two trifunctional phenylethynyl-terminated imide oligomers compared with the corresponding bifunctional structure. *Progress in Reaction Kinetics and Mechanism*, 41(1):1–13, 2016. arXiv:https://doi.org/10.3184/146867816X14544154610684, doi:10.3184/146867816X14544154610684.

[48] Jin Huang, Jiajia Zhou, and Mingjie Liu. Interphase in polymer nanocomposites. *JACS Au*, 2(2):280–291, 2022. arXiv:https://doi.org/10.1021/jacsau.1c00430, doi:10.1021/jacsau.1c00430.

[49] Lérys Granado, Stefan Kempa, Stefanie Bremmert, Laurence Gregoriades, Frank Brüning, Eric Anglaret, and Nicole Fréty. Isothermal dsc study of the curing kinetics of an epoxy/silica composite for microelectronics. *Journal of Microelectronics and Electronic Packaging*, 14:45–50, 04 2017. doi:10.4071/imaps.359903.

[50] Ralf Riedel, Gabriela Mera, Ralf Hauser, and Alexander Klonczynski. Silicon-based polymer-derived ceramics: Synthesis properties and applications-a review : Dedicated to prof. dr. fritz aldinger on the occasion of his 65th birthday. *Journal of the Ceramic Society of Japan*, 114:425–444, 2006. URL: https://api.semanticscholar.org/CorpusID:99307225.

[51] Richard A. Venditti and John K. Gillham. A relationship between the glass transition temperature (tg) and fractional conversion for thermosetting systems. *Journal of Applied Polymer Science*, 64:3–14, 1997. URL: https://api.semanticscholar.org/CorpusID:96615351.

[52] Hua Zou, Shishan Wu, and Jian Shen. Polymer/silica nanocomposites: Preparation, characterization, properties, and applications. *Chemical Reviews*, 108(9):3893–3957, 2008. PMID: 18720998. arXiv:https://doi.org/10.1021/cr068035q, doi:10.1021/cr068035q.

[53] Sergey Vyazovkin, Alan K. Burnham, José M. Criado, Luis A. Pérez-Maqueda, Crisan Popescu, and Nicolas Sbirrazzuoli. Ictac kinetics committee recommendations for performing kinetic computations on thermal analysis data. *Thermochimica Acta*, 520(1):1–19, 2011. URL: https://www.sciencedirect.com/science/article/pii/S0040603111002152, doi:10.1016/j.tca.2011.03.034.